Cells interpret temporal information from TGF-β through a nested relay mechanism

Jingyu Zhang[1,✦], Xiao-Jun Tian[1,✦], Yi-Jiun Chen[1], Weikang Wang[1], Simon Watkins[2], and Jianhua Xing[1]*

[1]Department of Computational and Systems Biology, School of Medicine, University of Pittsburgh, Pittsburgh, PA, 15260, USA

[2]Department of Cell Biology, School of Medicine, University of Pittsburgh, Pittsburgh, PA, 15260, USA

✦ The two contributed equally.

*To whom correspondence should be sent: xing1@pitt.edu

Abstract

The detection and transmission of the strength and temporal quality of intracellular and extracellullar signals is an essential cellular mechanism. While TGF-β signaling is one of the most thoroughly studied signaling pathways, the mechanisms by which cells translate TGF-β signals remain unclear. In this paper, through an integrated quantitative and computational approach we demonstrate that crosstalk among multiple TGF-β activated pathways forms a relay from SMAD to GLI1 that initializes and maintains SNAILl expression, respectively. This transaction is smoothed and accelerated by another temporal switch from elevated cytosolic GSK3 enzymatic activity to reduced nuclear GSK3 enzymatic activity. This nested relay mechanism places SNAIL1 as a key integrator of information from TGF-β signaling subsequently distributed through divergent pathways; essentially cells generate a transient or

1

22   sustained expression of SNAIL1 depending on TGF-β duration. Our results provide a

23   mechanistic understanding of a long-standing paradox that TGF-β can both suppress and

24   promote cancer development.

25   .

26   Keywords: TGF-β, SNAIL1, GLI code, GSK3, information flow,

27

28

Introduction

29

30   Cells live in as state of constant environmental flux and must reliably receive, decode, integrate

31   and transmit information from extracellular signals such that response is appropriate [1-4].

32   Dysregulation of signal transduction networks leads to inappropriate transmission of signaling

33   information which may ultimately lead to pathologies such as cancer. Therefore a central

34   problem in systems biology has been to untangle how cellular signal mechanisms are encoded

35   and decoded.

36   Cellular responses may have distinct temporal profiles. An adaptive response is transient, and the

37   system generally returns to the pre-stimulation state. An inflammatory response is a classical

38   example of this, where multiple levels of negative feedback and incoherent feed-forward loops

39   ensure final resolution and prevent chronic inflammatory responses [5]. In contrast a sustained

40   response may persist after removal of the original signal – typically through positive feedback

41   loops. Some cellular signals affect multiple cellular processes through a number of pathways and

42   induce both types of responses under different circumstances. However it remains an open

43   question as to how cells decide, generate and inter-convert between these different forms of

44   responses.

45   One example of multifunctional factor is the transforming growth factor-β (TGF-β), a secreted

46   protein that regulates both transient and persistent cellular processes such as proliferation,

47   morphogenesis, homeostasis, differentiation, and the epithelial-to-mesenchymal transition (EMT)

48   [6-10]. The multifunctional roles of TGF-β have challenged the central paradigm in endocrinology

49   that each hormone has a single functional role. Since its discovery in 1980s [11], researchers have

50   been puzzled by the enigma of "how cells read TGF-β signals", arising from seemingly

3

51 paradoxical observations seen when TGF-β acts as both inhibitor of pre-malignant cells and

52 promoter of invasion and metastasis in the later stage of tumor development [6, 7]. Because it plays

53 essential roles in developmental and normal physiological process, and its dysregulation is

54 related to cancer, fibrosis, inflammation, Alzheimer's disease and many other diseases, the TGF-

55 β signaling pathway has been probed extensively as a potential pharmaceutical target [12, 13].

56 However, this is difficult to do without understanding the seemingly dichotomous roles of TGF-

57 β.

58 To dissect this enigma we focused on one facet of this process: TGF-β induced SNAIL1

59 expression. SNAIL1 is a target of TGF-β signaling and plays a key role in regulating a number of

60 subsequent downstream processes. While most existing quantitative studies focus on the TGF-β-

61 SMAD axis [14-16], our results show that crosstalk between the SMAD-dependent and independent

62 pathways are key to understanding how cells decode and transmit temporal and contextual

63 information from TGF-β. We posit that the mechanism may be a central mechanistic signal

64 transduction process as many signaling pathways share the network structure.

65 **Results**

66 **The canonical TGF-β/SMAD/SNAIL1 pathway cannot explain two waves in SNAIL1**

67 **dynamics.**

68 Most existing knowledge as to how cells interpret TGF-β signals resides in the canonical TGF-β

69 pathway, where TGF-β leads to phosphorylation of SMAD2 and SMAD3 (pSMAD2/3),

70 followed by nuclear entry and action as a direct transcription factor for multiple downstream

71 genes [16, 17]. Among the regulatory targets of pSMAD2/3 is activation of its own inhibitor, I-

72 SMAD. pSMAD2/3 and I-SMAD create a negative feedback loop, which leads to only a

73   transient localization of pSMAD2/3 in the nucleus. pSMAD2/3 also promotes expression of

74   SNAIL1. Due to the double-negative feedback loops between SNAIL1 and miR-34 family

75   proteins, the expression of SNAIL1 is sustained after decay of nuclear pSMAD2/3. This

76   mechanism is supported by SMAD2/3 binding sites on the promoter region of snail1 [18].

77   Since quantifying SMAD proteins are the fundamental readouts of most current TGF-β signaling

78   studies, we set out to examine the downstream localization and abundance of SNAIL directly.

79   Human MCF10A cells were treated with recombinant TGF-β1 and multicolor

80   immunofluorescence (IF) was performed using antibodies directed against pSMAD2/3, SNAIL1.

81   As expected pSMAD2/3 proteins accumulated in the nucleus transiently, peaking at 12 hours

82   after TGF-β1 treatment, followed by a decrease by 24 hours (Fig. 1B & C). We confirmed the

83   transient pSMAD2/3 dynamics by sampling 1100-2600 cells at each time point (Fig. 1C). The

84   result is consistent with reports in the literature [14, 16, 19], and supports the theoretical prediction of

85   a negative feedback loop. Interestingly SNAIL1expression showed an additional twist to the

86   theoretical prediction of a sustained response. In our experiments nuclear SNAIL1 concentration

87   rose concurrently with pSMAD2/3 (Fig. 1B & C), then there was a surprising and transient dip at

88   24 hours, followed by another increase followed by a persistant elevation for one week [20].

89   Importantly this is not cell type dependent as equivalent two-wave dynamics were seen for

90   *SNAIL1* mRNA in MCF10A (Fig. 1D), MCF7 and A549 cells (Fig S1B), suggesting there may

91   be a secondary activator of SNAIL1.

92   To address the hypothesis that the activation of SNAIL1 is multifactorial and not solely

93   dependent on SMAD2/3 we treated MCF10A cells with a SMAD2/3 inhibitor LY2109761 in

94   addition to TGF-β treatment (Fig. 1D). When the inhibitor was added concurrently with TGF-β

95   treatment, the *SNAIL1* mRNA level was reduced to ~ 9% of that of the control (no inhibitor)

5

96   experiment by day 3, indicating that indeed pSMAD2/3 are required for SNAIL1 activation.

97   However, the *SNAIL1* mRNA level remained ~ 70% when the inhibitor was added 48 hours after

98   initiation of TGF-β treatment (when nuclear pSMAD2/3 concentration has dropped to a

99   minimum). Equivalent effects were seen with MCF7 and A549 cells (Fig. S1C). These results

100   reveal that pSMAD2/3 is essential for the early phase of SNAIL1 activation, but is less important

101   for the secondary phase elevation and persistence of SNAIL1 expression/localization.

102   One possible explanation is that the double-negative feedback loop between miR-34 and

103   SNAIL1 may reactivate SNAIL1 expression at day 2. However, our quantitative PCR

104   measurements revealed that reduction of miR-34 expression took place after day 2 ruling out this

105   possibility (Fig. S1D). Furthermore we performed a thorough parameter space search using a

106   multi-configuration Monte Carlo algorithm (Fig. S1E) over a mathematical model for the

107   network in Fig. 1A. The search revealed regions of the parameter space that quantitatively

108   reproduced the transient pSMAD2/3 dynamics, but not the two-wave dynamics of SNAIL1

109   expression (Fig. 1E). Therefore both experimental results and computational analysis strongly

110   suggest that the accepted mechanism shown in Fig. 1A is in fact incomplete, and there are one or

111   more missing links between TGF-β and SNAIL1.

112   **GLI1 is a signaling connector between SMAD and SNAIL1.**

113   Subsequently we performed network analysis and showed that SMAD-dependent and -

114   independent pathways may form a highly connected TGF-β signaling network (Fig. S2A), in

115   common with previous reports [21]. Our analysis identified GLI1, a key component of the

116   Hedgehog pathway, as a signaling hub in the network (Fig. 2A). TGF-β treatment can lead to

117   elevated GLI1 expression, either through transcriptional activation by pSMAD2/3, or through

118   degrading GSK3, while the latter facilitates GLI1 and SNAIL1 protein degradation [22, 23]. The

119   network integrates multiple feed-forward loops that converge at the regulation of SNAIL1

120   transcription. We therefore hypothesized that at the point when the SMAD ceases to function as

121   a major transcription factor of SNAIL1, it has already induced GLI1 expression, and that the

122   concentration of GLI1 may be sustained through positive feedback and continued induction via

123   other impactful TGF-β signaling pathways. Essentially, a relay from pSMAD2/3 to GLI1

124   initiates and then maintains SNAIL1 expression.

125   To test this hypothesis, we performed microscopy studies of SNAIL1-GLI1 using MCF10A cells.

126   The distribution of SNAIL1 found in this study (Fig. S2B) was consistent with those from the

127   pSMAD2/3-SNAIL1 studies. Elevated and sustained expression of GLI1 under TGF-β treatment

128   (Fig. 2B & C) was clearly evident. More interestingly GLI1 also showed an unexpected multi-

129   phasic dynamic. Around 8 hours after TGF-β treatment, cytosolic GLI1 concentration started to

130   increase. At 12 hours when SMAD activities decreased toward basal levels there was a clear

131   accumulation of GLI1 in the nucleus, which continued to increase through day 2. Notably, at

132   this time point cells expressing a high level of nuclear SNAIL1 consistently showed high

133   intranuclear concentrations GLI1 (Fig. S2B), strongly suggesting that the second wave of

134   SNAIL1 is caused by sustained GLI1 expression. Computational modeling of the network in Fig.

135   2A also reproduced the temporal dynamics of pSAMD2/3 and SNAIL1 (Figure S2C).

136   If GLI1 is involved in the maintenance of SNAIL1 expression subsequent to the drop in

137   pSMAD2/3 concentration, it is reasonable to predict (Fig. S2D) that inhibiting GLI1 activity,

138   either at the onset of or at some subsequent time after TGF-β treatment, would have minimal

139   effect on the initial wave of SNAIL1 expression since it is caused by pSMAD2/3. However, it

140   would eliminate the second wave of SNAIL1 expression. Indeed this was observed when the

141   GLI1 inhibitor GANT61 was added together with TGF-β at the beginning of the experiment

7

142   resulting in a reduction of the *SNAIL1* mRNA level to be 55% (at 12 h and 24 h), 12% (at 48 h)

143   and 7% (at 72 h) compared to those without inhibition at the corresponding time points.   In

144   another experiment adding the inhibitor 48 hours after TGF-β treatment also reduced the mRNA

145   level measured at 72 h to be 25% (Fig. 2D). These results are qualitatively different from those

146   with the SMAD inhibitor (Fig. 1D).

147   To confirm that GLI1 activation is not restricted to the MCF10A cell line, we also examined

148   MCF7 and A549 cells with TGF-β treatment, and observed similar increased and sustained GLI1

149   expression (Fig. S2E). Furthermore, early and late GLI1 inhibition lead to a reduction of the

150   *SNAIL1* mRNA level to be 13% and 22% for MCF7 cells, and to a less extent of 57% and 66%

151   for A549 cells, respectively (Fig. S2F). Additionally, increased GLI1 expression after TGF-β

152   treatment has been found for multiple liver cancer cell lines [24]. *In toto* these results support the

153   potential role of GLI1 as a signaling relay from pSMAD2/3 to SNAIL1.

154   **GSK3 in a phosphorylation form with augmented enzymatic activity accumulates at**

155   **endoplasmic reticulum and Golgi apparatus.**

156   Next, we hypothesized that GSK3 is fundamental to the observed multi-phasic GLI1 dynamic

157   (Fig. 2). Most published studies suggest that GSK3 is constitutively active in untreated cells,

158   facilitating degradation of SNAIL1 and GLI1; TGF-β treatment leads to GSK3 phosphorylation

159   and inactivation, which leads to an accumulation of SNAIL1 and GLI1 [25, 26].

160   Initially we tested whether the above mechanism is sufficient to explain the multi-phasic GLI1

161   dynamics. We treated MCF10A cells in the absence of TGF-β with a GSK3 inhibitor that

162   suppresses GSK activity without interfering with its phosphorylation. Given the above

163   mechanism, one should expect the GSK3 inhibitor to promote both GLI1 and SNAIL1. In our

164   experiment, SNAIL1 did increase, but there was no change in GLI1 expression in either nucleus

8

165   or cytoplasm (Fig. 3A), suggesting additional signaling mechanisms may be involved.

166   Besides the inhibitory serine phosphorylation, the literature suggests that tyrosine (Y279 in

167   GSK-3α and Y216 in GSK-3β) phosphorylation leads to augmented enzymatic activity of GSK3

168   [27]. As a convenience when discussing the three forms of GSK3, we refer the enzymatically active

169   unphosphorylated form and the more active tyrosine phosphorylated form as "GSK3^A" and

170   "GSK3^{AA}", respectively, and the inactive serine phosphorylation form as "GSK3^D". Also we

171   reserve "GSK3" for the total GSK3. As expected, microscopy studies showed an increased

172   concentration of GSK3^D peaking around 12 hours after TGF-β treatment (Fig. 3B, Fig. S3A).

173   Large cell-to-cell variations in the concentration of GSK3^D were observed, however, the

174   abundance of cytosolic and nuclear GSK3^D were essentially equivalent (the expression ratio was

175   close to one) for cells without TGF-β treatment (Fig. S3B). This observation corroborates earlier

176   report that the serine phosphorylation does not affect GSK3 nuclear location [28]. TGF-β treatment

177   led to transient deviation of this ratio from equivalence, reflecting additional active and dynamic

178   regulation of GSK3 including covalent modification, location and protein stability. Specifically

179   prior to inhibitory serine phosphorylation we observed transient GSK3^{AA} accumulation in the

180   perinuclear region peaking at eight hours (Fig. 3B, Fig. S3A). Close examination of higher

181   magnification confocal images revealed that the GSK3^{AA} formed clusters in the endoplasmic

182   reticulum (ER) and Golgi apparatus, but not associated with actin filaments (Fig. 3C, Movie 1 &

183   2). Given that a function of active GSK3 is to modify target proteins post-translationally, our

184   observation suggests an unreported role for GSK3^{AA} accumulating at the ER and Golgi apparatus

185   is to modify newly synthesized proteins before their release to the cytosol. Specifically previous

186   studies showed that in mammalian cells a scaffold protein SUFU binds to GLI to form an

187   inhibitory complex, and SUFU phosphorylation by GSK3β prevents the complex formation,

9

188   exposes the GLI1 nuclear localization sequence [29], which explains the observed increase of free

189   GLI1 in the cytosol followed by nuclear translocation (Fig. 2B). Since the two phosphorylation

190   forms, GSK3^{AA} and GSK3^{D}, coexist within single cells at defined time points, we performed co-

191   immunoprecipitation and found that the probability of having the two GSK3 phosphorylation

192   forms in one molecule was undetectable (Fig. S3C).

193   Contrary to our observation that TGF-β regulates GSK3^{AA} dynamics, other studies posit that

194   GSK3^{AA} is not regulated by external cues [30]. To resolve this paradox, we measured the relative

195   amount of different GSK3 forms through silver staining (Fig. S3D). Among the three forms, the

196   overall percentage of GSK3^{D} increased from a basal level of 37% to 65% at 12 h after TGF-β

197   treatment. In contrast, only a small fraction of GSK3 molecules assumed the GSK3^{AA} form and

198   its overall abundance was stable over time (from ~10% basal level to ~13% at 8 h then back to

199   ~10% at 12 h after TGF-β treatment). Essentially levels of GSK3^{AA} did not change in abundance

200   but did change in localizations (homing to the ER and Golgi apparatus) to form a high local

201   concentration, which imbue an important role in TGF-β signaling.

202   **A temporal and compartment switch from active to inhibitory GSK3 phosphorylation**

203   **smooths the SMAD-GLI1 relay and reduces cell-to-cell heterogeneity on GLI1 activation.**

204   Based on the above results, we constructed an expanded network for TGF-β induced SNAIL1

205   expression, which integrates a role for GSK3 and its switching among the three phosphorylation

206   forms as well as a functional role due to its intracellular redistribution (Fig. 4A). The model

207   reproduces the multiphasic dynamics of GLI1 as well as that of pSMAD2/3 and SNAIL1 (Fig.

208   S4A).

209   To understand the function of the early nuclear accumulation of GLI1 induced by GSK3^{AA} , it is

210   important to recognize that GLI1 has a positive-feedback loop, and this network motif (Fig. 4B,

10

211   left panel) has characteristic sigmoidal shaped temporal dynamics, with the substrate

212   concentration increasing slowly at first then accelerating with time until it approaches saturation

213   (Fig. 4B, right panel, red curve). The response time, t_R, defined as the time taken to reach a target

214   concentration value $[X]_R$, is highly sensitive to initial substrate concentration $[X]_0$: in fact a slight

215   increase in the initial concentration, $\Delta[X]$, will significantly shorten response time (Fig. 4B, right

216   panel, blue curve), and for a fixed $\Delta[X]$ a greater acceleration is seen in cells with lower initial

217   concentrations (Fig. 4B, right panel, inlet figure). Consequently despite variations of their initial

218   concentration of X, most cells within a population can reach $[X]_R$ by a targeted time point t_T in a

219   series of temporally regulated events such as cell differentiation and immune response. The

220   needed concentration boost may be effected by conversion of preformed molecules from an

221   inactive form into an active form (Fig. 4B, left panel, the part of the network in green). Indeed,

222   many examples of this modified feedback loop motif exist. Figure S4B gives some examples

223   involving members of intrinsically disordered proteins and inhibitors of DNA binding proteins,

224   β-catenin and the STING motif for immune responses. In the present scenario the accelerated

225   GLI1 dynamic ensures sufficient accumulation of GLI1 before nuclear pSMAD2/3 level

226   decreases, essentially analogous to a relay race when the first runner can only release the baton

227   after the second runner has grabbed it. Later when the GLI1 and SNAIL1 concentrations start to

228   increase, the $GSK3^A \rightarrow GSK3^D$ conversion became necessary to reduce the rates of their

229   degradation catalyzed by active GSK3. Interestingly, this conversion takes place concurrently

230   with maximal concentration of nuclear pSMAD2/3, which activates GLI1 and SNAIL1

231   transcription. Furthermore, the small initial concentration boost does not affect another major

232   function of the positive feedback loop, which is to robustly buffer fluctuations in signal strengths

233   via bistable dynamics (Fig. S4C).

11

234   To test the functional roles of GSK3 suggested above, we performed a series of GSK3 activity

235   inhibition experiments. First, we pretreated MCF10A cells with GSK3 inhibitor SB216763,

236   washed out the inhibitor then added TGF-β1 (Fig. S4B). We predicted that the treatment would

237   slow down GLI1 nuclear accumulation, and at later times decrease the overall increase of GLI1

238   and SNAIL1 compared to cells without GSK3 inhibitor. Indeed this was observed (Fig. 4C,

239   TGF-β +/- GSK3_I). More interestingly, the scatter plots show the distributions with and without

240   the inhibitor are similar in cells with high GLI1, but in the presence of inhibitor there is a

241   population of non-responsive cells with low GLI1 and SNAIL1. This observation is consistent

242   with the model prediction that the GSK3-induced boost of initial GLI1 concentration leads an

243   acceleration in the response time for cells with lower initial nuclear GLI1 concentration (Fig. 4B,

244   right panel). In a separate experiment (Fig. S4C), we did not wash out GSK3 inhibitor while

245   adding TGF-β. In this case the inhibitor had opposite effects on the GLI1/SNAIL1 protein

246   concentration: it slowed down the initial release and translocation of GLI1 needed to accelerate

247   the GLI1 accumulation, but also decreased GLI1 and SNAIL1 degradation that becomes pre-

248   eminent when the proteins were present at high levels. Compared to the samples grown in the

249   absence of the GSK3 inhibitor, we also observed slower and more scattered GLI1 nuclear

250   accumulation and SNAIL1 increase on day 2, but by day 3 the overall levels of GLI1 and

251   SNAIL1 were actually higher than the case without the inhibitor (Fig. 4C, TGF-β + GSK3_I).

252   **The SMAD-GLI1 relay increases the network information capacity and leads to**

253   **differential response to TGF-β duration**

254   Our results show that TGF-β1 signaling is effected through pSMAD2/3 directly with fast pulsed

255   dynamics concurrently with a relay through GLI1 which has a much slower dynamics. The

256   signaling ported by these two channels converges on SNAIL1 with a resultant two-wave

12

257   expression pattern. To further dissect the potential functional interactions between these two

258   pathways, we performed mathematical modeling and predicted that the two distinct dynamics

259   allows cells to respond to TGF-β differentially depending on stimulus duration (Fig. 5A). Short

260   pulses of TGF-β only activate pSMAD2/3 and the first wave of transient SNAIL1 expression.

261   When the signal duration is longer than a defined threshold value, activation of GLI1 will lead to

262   the observed second wave of SNAIL1 expression. We confirmed the predictions with MCF10A

263   cells (Fig. 5B). Both TGF-β1 pulses with duration of two hours and eight hours activated

264   pSMAD2/3 and the first wave of SNAIL1 expressions. However, only the eight-hour but not the

265   two-hour pulse activated sustained GLI1 and the second wave of SNAIL1 expression, similar to

266   those with continuous TGF-β1 treatment.

267   Clearly cellular responses have different temporal profiles depending on the TGF-β duration, and

268   one can use the information theory to quantify their information content [31, 32]. In this study we

269   utilized a more intuitive understanding of network function from an information encoding

270   viewpoint. Consider the pSMAD complex, which has three coarse-grained states, High (H),

271   Medium (M), and Low (L), and each of GLI1 and SNAIL1 has two states, H and L (Fig. 5C).

272   Then one can use three 4-element states, (L, L; L, L), (H, L; L, L), (H, M; L, H) to roughly

273   describe the case without TGF-β and the 8 hour and 12 hour pulse results in Fig. 5B, where each

274   number in a state represents in the order the 12 h and 48 h concentrations of pSMAD2/3 and

275   GLI1, respectively. The three states are part of a temporally ordered state space, and encode

276   information of TGF-β duration roughly as not detectable, short, and long. The same information

277   is encoded by the SNAIL1 dynamics as (L, L), (H, L), and (H, H), reflecting SNAIL1 as an

278   information integrator of the two converging pathways.

279   Further modeling suggests that components in the network function cooperatively to encode the

280   TGF-β information (Fig. S5A). Increasing or decreasing the nuclear GSK3 enzymatic activity

281   tunes the system to generate the second SNAIL1 wave with a higher or lower threshold of TGF-β

282   duration, respectively, while changing the cytosol GSK3 enzymatic activity has the opposite

283   effect. Upregulation of GLI1, or downregulation of I-SMAD, both of which have been observed

284   in various cancer cells, also decrease the threshold for generating the second SNAIL1 wave.

285   Therefore cells of different types can share the same network structure, but fine-tune their

286   context-dependent responses by varying some dynamic parameters, and for a specific type of

287   cells dysregulation of any of the signaling network components may lead to misinterpretation of

288   the quantitative information of TGF-β signal.

Discussion

289

290   TGF-β is a multifunctional cytokine that can induce a plethora of different and mutually

291   exclusive cellular responses. Despite the growing number of studies related to TGF-β signaling,

292   it remains enigmatic how cells interpret the signal. It is suggested that one factor contributing to

293   this complexity comes from the fact that TGF-β can activate a number of pathways

294   interconnected with multiple crosstalk points. Our studies reveal that this interconnection is

295   essential such that components of the network can function coordinately and appropriately to

296   interpret the temporal (time and duration) information from TGF-β.

297   **pSMADs are major inducers for the first wave of SNAIL1 expression.**

298   The two-wave dynamic of TGF-β-induced SNAIL1 expression has been observed in several

299   cellular systems [21, 33], supporting the underlying relay mechanism discovered in this work. The

300   first wave is fundamentally induced by pSMAD2/3, as evidenced from our SMAD inhibition

14

301　experiments, and similarity between the dynamics of pSMAD2/3 and the first wave of SNAIL1.

302　SNAIL1 may act as cofactor of pSMADs to induce other early response genes [34]. At later times

303　the nuclear concentrations of pSMAD2/3 decrease though continue to contribute to SNAIL1

304　activation at a lower level.

305　**GLI1 is a signaling hub for multiple pathways and temporal checkpoint for activating**

306　**second-wave of sustained SNAIL1 expression.**

307　GLI protein has been traditionally attributed to the canonical Hedgehog pathway. Here we show

308　that TGF-β induction of GLI1 relays the signal to induce SNAIL1. Consistent with the present

309　study, Dennler et al. reported SMAD3-dependent induction of the GLI family by TGF-β both in

310　multiple cultured cell lines, and in transgenic mice overexpressing TGF-β [22] Many other signals

311　such as PGF, EGF can also activate the GLI family, and a GLI code has been proposed to

312　integrate input from different pathways and lead to context-dependent differential responses [35].

313　Our results confirmed this role of GLI1 as an intermediate information integrator and transmitter,

314　and suggest that both the strength and duration of the TGF-β stimulation are important, and must

315　act above threshold concentrations and durations to activate the second wave of SNAIL1. This

316　temporal and strength checkpoint prevents spurious SNAIL1 activation and subsequent major

317　cellular fate changes.

318　**GSK3 fine-tunes the threshold of the GLI1 checkpoint and synchronizes responses of a**

319　**population of cells**

320　The functional switch from pSMAD2/3 to GLI1 relays information from TGF-β signaling

321　beyond the initial induction of SNAIL1, and this relay is facilitated by a second relay from the

322　active to the inactive phosphorylation form of GSK3 proteins. Active regulation of the

323　abundance and nuclear location of GSK3^{AA} form has been observed in neurons [36]. In contrast to

15

324   these earlier reports we observed an accumulation of GSK3[AA] in the ER and Golgi apparatus.

325   Mechanistically this may be caused by redistribution of cytosolic GSK3[AA], or a simple

326   accumulation of *de novo* synthesized and phosphorylated GSK3 proteins. The overall

327   consequence is an increase in local GSK3 enzymatic activity, which forms part of the GSK3

328   switch that smooths the pSMAD2/3-GLI1 transition and the duration threshold of TGF-β pulse

329   that generates the second wave of SNAIL1.

330   This seemingly simple process, which accelerates the response time through transient and minor

331   increases in the initial concentration of a molecular species subject to positive feedback control,

332   may have profound biological functions. Positive feedback loops are ubiquitous in cellular

333   regulation, with a major function to filter both the strength and temporal fluctuations of

334   stimulating signals and to prevent inadvertent cell fate change. This network, however, may

335   have an inherently slow response time, and the response is highly sensitive to initial conditions

336   that lead to large cell-to-cell variation of temporal dynamics. This variation and slow dynamic

337   may be problematic for processes such as neural crest formation and wound healing where

338   precise and synchronized temporal control is crucial for generating collective responses of

339   multiple cells. Transient increases in initial protein concentrations of the GSK3 module may

340   solve the seemingly incompatible requirements for the motif on robustness against fluctuations

341   as well as fast and synchronized responses. It assures that despite a possible broad distribution of

342   basal expression levels of the protein, cells are activated within a designated period of time at the

343   presence of persistent activation signal, without scarifying the filtering function of the feedback

344   loop.

345   **Cells use a temporally ordered state space formed by a composite network to increase**

346   **information transfer capacity.**

16

347 Cells constantly encounter TGF-β signals with different strengths and duration, and must

348 respond accordingly. It is well documented that biological networks reliably transmit information

349 about the extracellular environment despite intrinsic and extrinsic noise in a subtle and functional

350 way. However, quantitative analyses using information theory reveal that the dynamic of each

351 individual readout is quite coarse with one or few bits [31, 32]. This is a paradox. However, our

352 results suggest that cells use multiple readouts to generate a temporally ordered state space with

353 an expanded capacity to encode signal information and generate a far more subtle response

354 system. For example, the SMAD motif has a refractory period due to the negative feedback loop

355 and thus can accurately encode the duration information of TGF-β only within a limited temporal

356 range, then the GLI1 motif encodes information of longer TGF-β duration which then saturates.

357 This temporally ordered state network may be further expanded, such that the SNAIL1 motif

358 itself possibly encodes information of longer TGF-β duration and relays to other transcription

359 factors such as TWIST and ZEB, and lead to stepwise transition from the epithelial to the

360 mesenchymal phenotype depending on the TGF-β duration [20].

361 As with other signaling process, TGF-β signaling is context dependent, and the dynamic and

362 regulatory network vary between cell types [15, 37]. For the three cell lines we examined our results

363 identify GLI1 as a major relaying factor for the TGF-β signaling. The inhibition experiments

364 show that other possible peripheral links have minor contributions to SNAIL1 activation, while

365 their weights may grow at time later than we examined. Consequently the present work has

366 focused on the early event of TGF-β activation of SNAIL1, which is with 72 h for MCF10A

367 cells. Nevertheless, the relay mechanism and the corresponding network structure identified here

368 can be general for transmitting quantitative information of TGF-β and other signals. It is typical

369 that an extracellular signal is transmitted through a canonical pathway with negative feedbacks

17

370   and multiple non-canonical pathways, and these pathways crosstalk at multiple points, and Fig.

371   S5B gives some examples including IL-12, DNA double strand breaking, and LPS. Therefore the

372   mechanism revealed in this work is likely beyond TGF-β signaling.

373   **Abnormal upregulation of GLI1 dysregulates SNAIL1 activation and changes TGF-β from**

374   **tumor suppressor to metastasis promoter.**

375   Returning to the TGF-β paradox mentioned in the introduction. Our results revealed a network

376   which integrates several factors that work cooperatively to interpret the temporal information of

377   TGF-β and generate distinct SNAIL1 expression patterns. Franco et al. showed that SNAIL1

378   suppresses TGF-β induced apoptosis and promotes [38]. In premalignant cells such as MCF10A

379   cells GLI1 still functions close to normal as a temporal checkpoint of TGF-β on inducing

380   SNAIL1 activation, thus TGF-β serves as a tumor suppressor by inducing apoptosis through the

381   SMAD-dependent pathway. On the other hand, GLI1 is upregulated in many types of cancer and

382   the MCF7 and A549 cells we studied (28), so under TGF-β stimulation these cancer cells are

383   prone to SNAIL1 activation and EMT instead of apoptosis.

384   **Network temporal dynamics is a key for effective pharmaceutical intervention.**

385   Upregulation of GLI1, and GSK3 and the responsive SMAD family has been reported in

386   pathological tissues of fibrosis [39]and cancer [35], and all three have been considered as potential

387   drug targets. The present study emphasizes that in cell signaling timing is fundamental to

388   function. The same network structure may generate drastically different dynamics with different

389   parameters, as observed for different cell types. Consequently, effective biomedical intervention

390   needs to take into account the network dynamics. We have already demonstrated that adding the

391   inhibitors at different stages of TGF-β induction can be either effective versus not effective on

392   reducing SNAIL1 (by inhibiting pSMAD2/3), both effective (by inhibiting GLI1), and even

18

393 opposite (by inhibiting GSK3). Actually, one may even exploit this dynamic specificity for

394 precisely targeting certain group of cells while reducing undesired side effects on other cell types.

395 In summary through integrated quantitative measurements and mathematical modeling we

396 provided a mechanistic explanation for the long-time puzzle of how cells read TGF-β signals.

397 Several uncovered specific mechanisms, such as expanding information transmission capacity

398 through signal relaying, and reducing response times of positive feedback loops by increasing

399 initial protein concentrations, may be general design principles for signal transduction.

Methods

Cell Culture

402 MCF10A cells were purchased from the American Type Culture Collection (ATCC) and

403 were cultured in DMEM/F12 (1:1) medium (Gibco) with 5% horse serum (Gibco), 100 μg/ml of

404 human epidermal growth factor (PeproTech), 10 mg/ml of insulin (Sigma), 10 mg/ml of

405 hydrocortisone (Sigma), 0.5 mg/ml of cholera toxin (Sigma), and 1x penicillin-streptomycin

406 (Gibco). MCF7 cells were purchased from ATCC and cultured in EMEM medium (Gibco) with

407 10% FBS (Gibco), 10 mg/ml of insulin, and 1x penicillin-streptomycin. A549 cells were

408 purchased from ATCC and were cultured in F12 medium (Corning) with 10% FBS and 1x

409 penicillin-streptomycin. All cells were incubated at 37 °C with 5% CO_2.

TGF-β induce and inhibitor treatment

411 Cells for TGF-β induction and inhibitor treatment were seeded at ~60-70% confluence without

412 serum starvation. For TGF-β treatment, 4 ng/ml human recombinant TGF-β1 (Cell signaling)

413 was added into culture medium directly. For inhibition experiment, 4 μM of LY2109761

414 (Selleckchem), 20 μM of GANT61 (Selleckchem), and 10 μM of SB216763 (Selleckchem) were

19

415   used to inhibit SMAD, GLI and GSK3, respectively. The medium was changed every day during

416   treatment to keep the reagent concentration constantly. For reproducibility, we used cells within

417   10th -15th generations, same patches of reagents, serum, and tried to perform each group of

418   experiments (e.g., those in Fig. 1C) together.

419   **Immunofluorescence Microscopy and Data Analysis**

420   Cells were seeded on four-well glass-bottom petri dishes at ~60% confluence overnight and

421   treated with reagents (TGF-β1 and/or inhibitors). Three independent experiments were

422   performed in every treatment. At designated time points, cells were harvested and stained with

423   specific antibodies following procedure modified from the protocols at the Center of Biological

424   Imaging (CBI) in the University of Pittsburgh. In general, cells were washed with DPBS for five

425   minutes for three times followed by 4% formaldehyde fixation for 10 minutes at room

426   temperature. Cells were then washed three times with PBS for five minutes every time. PBS with

427   0.1% TritonX-100 (PBS_Triton) was used for penetration. BSA of 2% in PBST was used for

428   blocking before staining with antibodies. The first antibodies were diluted by PBST with 1%

429   BSA. Samples were incubated with the first antibodies at 4°C overnight. Then cells were washed

430   three times with 10 minutes for each before being incubated with the secondary antibodies for

431   one hour at room temperature. After antibody incubation, cells were washed with PBS_Triton for

432   five minutes and stained with DAPI (Fisher) for 10 minutes at room temperature. Cells were

433   washed with PBS_Triton for five minutes three times and stored in PBS for imaging.

434   Photos were taken with Nikon A1 confocal microscopy at CBI. The microscope was controlled

435   by the build-in software, Nikon NIS Elementary. All photos, except the photo for GSK3[AA]

436   subcellular localization, were taken with plan fluor 40x DIC M/N2 oil objective with 0.75

437   numerical aperture and 0.72 mm working distance. The scan field were chosen randomly all over

438 the glass-bottom area. For identifying the GSK3^{AA} subcellular localization, plan apo λ 100x oil

439 objective with 1.45 NA and 0.13 mm WD was used. The 3D model of GSK3^{AA} overlapped with

440 ERC and DAPI were reconstructed from 25 of z-stack images in 11.6 μm and videos were

441 produced also by NIS Element software. To minimize photobleaching, an object field was firstly

442 chosen by fast scan, then the photos were taken at 2014 × 2014 pixel or 4096 × 4096 pixel

443 resolution, for generation large data or for photo presentation, respectively.

444 CellProfiller was used for cell segregation and initial imaging analysis as what described in Carpenter

445 et.al. [40].

446 *Image Correction*. To keep identical background through all images, background correction was

447 performed before further image processing. For each image fluorescent intensities in space without cells

448 were used as local background. Photos that have obviously uneven illumination and background

449 fluorescence were removed from further processing. Otherwise the mean background fluorescent intensity

450 was obtained through averaging over the whole image, and was deducted uniformly from the image.

451 *Image Segmentation.* Cell number and position were determined by nuclear recognition with DAPI. The

452 global strategy was used to identify the nuclear shape, and the Otsu algorithm was used for further

453 calculation. Clumped objectives were identified by shape and divided by intensity. Next, using the shrank

454 nuclear shape as seed, cell shape was identified by the Watershed algorithm. For identifying the clusters

455 of GSK3^{AA} formed around a nucleus, the nuclear shape was shrank manually by 3 pixels and used as a

456 new seed to grown the boundary with the watershed method until reaching background intensity level. All

457 parameters were optimized through an iterative process of automatic segmentation and manual inspection.

458 *Image quantification*. Averaged fluorescence density and integrated fluorescence intensity were

459 calculated automatically with CellProfiler. The amount of the GSK3^{AA} form was quantified as the sum of

460 intensities of pixels belonging to the cluster formed around a nucleus. Concentrations of all other proteins

461 were quantified by the average pixel intensity within the nucleus or cytosol region of a cell. Next, the

462 quantified results were examined manually, and those cells with either cell area, nuclear area, or

463 fluorescent intensity beyond five folds of the 95% confidence range of samples from a given treatment

464 were discarded, which account for less than 1% of the cells analyzed. Immunofluorescence data were

465 further processed and plots were generated using customized R codes and Matlab codes. The R package [2],

466 was also used in data analysis.

467 **Quantitative PCR**

468 Cells were seeded in 12-well plastic bottom cell culture plates and treated as described above. Three

469 parallel experiments were performed in every treatment. Total RNA was isolated with the TRIZOL RNA

470 isolation kit (Fisher), and mRNA was reversely transcribed with the RNAscript II kit (ABI). The stem-

471 loop method was used for microRNA reverse transcription. The qPCR system was prepared with the

472 SYBR green qPCR kit with designed primers (Supplementary table 1) and performed on StepOnePlus

473 real-time PCR (ABI).

474 **Immunoprecipitation and silver staining**

475 Immunoprecipitation was performed with SureBeads magnetic beads (Bio-Rad) following a protocol

476 modified from the one provided by the manufacture. We washed beads with PBS with 0.1% Tween 20

477 (PBS_Tween) for three times, then harvested cells by RIPA (Thermo) with proteinase and phosphatase

478 inhibitor (Roche). Samples were pre-cleaned with 100 μl of suspended Protein G per 450 μl of lysis

479 mixture. Antibodies targeting GSK3 (Cell Signaling), GSK3AA (Santa Cruz), and GSK3D (Santa Cruz)

480 were added into every 100 μl of bead mixture respectively. The mixture was rotated at 4 °C for 3 hours.

481 Beads that were conjugated with antibodies were washed with PBS_Tween. An amount of 100 μl of pre-

482 cleaned lysis buffer was added into conjugated beads and rotated at 4 °C overnight. Targeted proteins

483 were eluded from beads by incubating with 40 μl 1x Laemmli buffer with SDS at 70 °C for 10 minutes.

484 For the samples an amount of 5 μl was used for western blot assay, and an amount of 30 μl was loaded

485 for SDS-PAGE (Bio-Rad) and followed by silver staining (Fisher).

22

Network reconstruction and coarse-graining

The full network from TGF-β1 to SNAIL1 (Fig. S2A) was generated with IPA (Qiagen®). Specifically, all downstream regulators of TGF-β1 and upstream regulators of SNAIL1 in human, mice and rat were searched and added to the network. Then, direct or indirect relationships between every pair of regulators were searched and added to the network. After obtaining the whole network, regulators that have been reported to be activated later than SNAIL1 were removed. Examination of the network reveals that the network can be further organized into three groups: the TGF-β-SMAD-SNAIL canonical pathway, the TGF-β-GSK3-β-catenin pathway that has the most number of links, and others. We further noticed that GLI1 is a central connector of TGF-β, SMAD, GSK3 and SNAIL1. We performed western blot studies on β-CATENIN and found that neither its concentration nor its location changes significantly before day 3, therefore we removed β-CATENIN from the network. In addition, previous studies report that the SMAD-GLI axis plays important role in TGF-β induced EMT [23]. Therefore we further grouped the network as the SMAD module, the GLI module, and the GSK3 module, as well as the remaining ones that we referred as "Others", and reached the network shown in Fig. 2A. Those molecular species not explicitly specified in Fig. 2A either have their effects implicitly included in the links, for example the link from TGF-β to GSK3, or are included in the links of "Others". This treatment is justified since our various inhibition experiments indeed showed that the three factors we identified affect SNAIL1 expression the most. These "other" species may contribute to snail1 activation at a time later than what considered in this work. Therefore we emphasize the network in Fig. 2A is valid only within the time window we examined, i.e., within three days after TGF-β1 treatment for MCF10A cells.

Acknowledgements

Figure Caption

Figure 1 Temporal gap exists between SMADs and SNAIL1 in response to TGF-β. (A) Canonical SMAD-dependent pathway for TGF-β activation of SNAIL1. (B) Two-color immunofluorescence (IF) images of pSMAD2/3 and SNAIL1 of MCF10A cells induced by 4 ng/ml TGF-β1 at various time points. The scale bar is 10 μm. Same for other IF images in this paper. (C) Distributions of nuclear pSMAD2/3 and SNAIL1 concentrations quantified from the IF images. Red vertical lines indicate the mean value of the distributions at time 0, and blue vertical lines represent that at 12 h (for pSMAD2/3) or at 48 h (for SNAIL1), respectively. The number on each figure panel is the number of randomly selected cells used for the analysis. Throughout the paper we report fold changes of concentration and amount relative to the mean basal value of the corresponding quantity. (D) Effects of early (added together with TGF-β) and late (48 h after adding TGF-β) pSMAD inhibition on the *SNAIL1* mRNA level. (E) Thorough parameter space search confirmed that with the model in panel A one can fit the pSMAD2/3 dynamics, but not the two-wave SNAIL1 dynamics. The experimental data are shown as violin plots with the medians given by black bars. Solid curves are computational results with parameter sets sampled from the Monte Carlo search, and the red curves are the best-fit results.

24

529

530 **Figure 2 Both network analysis and experimental studies revealed GLI1 as a key temporal**

531 **connector of TGF-β induced SNAIL1 expression**. (A) Reconstructed literature-based pathway

532 crosstalks for TGF-β induced SNAIL1 expression. The node "Others" refer remaining SNAIL1

533 activation pathways that have minor contributions to the time window under study and thus are

534 not explicitly treated. (B) IF images on protein levels of GLI1 (in the free form). Red and blue

535 vertical lines indicate the mean values of the distributions at time 0 and at 48 h, respectively. (C)

536 Distributions of nuclear GLI1 concentrations quantified from the IF images. **(D)** Effects of early

537 (added together with TGF-β) and late (48 h after adding TGF-β) GLI1 inhibition on the *SNAIL1*

538 mRNA level.

539 **Figure 3 TGF-β induced temporal switch between active and inhibitive phosphorylation**

540 **forms of GSK3 proteins.** (A) IF images showed that inhibiting GSK3 enzymatic activity alone

541 increased SNAIL1 accumulation but did not recapitulate TGF-β induced GLI1 nuclear

542 translocation. (B) Quantification of the IF images of MCF10A cells at different time points after

543 TGF-β treatment. Red vertical lines indicate the mean value of the distributions at time 0, and

544 blue vertical lines represent that at 8 h (for GSK3^{AA}) or at 12 h (for GSK3^{D}), respectively. (C) IF

545 images showing GSK3^{AA} localization at the endoplasmic reticulum center (ERC). (D) Proposed

546 network of the GSK3 module.

547

548 **Figure 4 The GSK3 phosphorylation switch smoothens the SMAD-GLI1 relay.** (A)

549 Proposed expanded network for TGF-β induced SNAIL1 expression. (B) Schematic of a generic

550 positive feedback loop network. Also shown in green is an additional reservoir of the molecules

551 in inactive form (X$_I$) that can convert quickly into the active form (X) upon stimulation. (C) The

25

552   response time t_R is sensitive to the initial concentration, $[X]_0$ v.s. $[X]_0 + \Delta[X]_0$. The inlet figure

553   shows the dependence of Δt_R on $[X]_0$ with $\Delta[X]_0$ fixed. (C-D) Box and scattered plots of GSK3

554   inhibition experimental data. On the right panel red points are the center of the scattered plots

555   and each ellipse encloses 97.5% of the data points. Both were drawn with the R package,

556   *car::data.ellipse*.

557

558   **Figure 5 The TGF-β-SNAIL1 network permits detection of TGF-β duration and**

559   **differential responses.** (A) Model predictions that the network generates one or two waves of

560   SNAIL1 depending on TGF-β duration. (B) Single cell protein concentrations quantified from IF

561   images of cells under pulsed and continuous TGF-β treatments. The solid lines divide the space

562   into coarse-grained states with respect to the corresponding mean values without TGF- β

563   treatments (= 1). (C) Schematics of how cells encode information of TGF-β duration through a

564   temporally ordered state space.

565

566   **Figure S1 Supplemental results showing the gap between pSMAD2/3 and SNAIL1**

567   **dynamics.** (A) Scattered plot of the 2D-IF imaging data. (B) Fold change of targeted gene

568   mRNA levels in MCF7 and A549 cells measured with quantitative RT-PCR after TGF-β1

569   treatment. (C) Fold change of targeted gene mRNA levels measured with quantitative RT-PCR

570   after combined TGF-β1 and SMAD2/3 inhibitor LY2109761 treatment. For early inhibition the

571   inhibitor was added at the time of starting TGF-β1 treatment. For late inhibition the inhibitor was

572   added 48 h (for MCF7) and 24 h (for A549) after starting TGF-β1 treatment, respectively. (D)

573   Fold change of miR-34a level in MCF10A cells measured with quantitative RT-PCR after TGF-

574   β1 treatment. (E) Schematic of the parameter space search approach.

575

576   **Figure S2 Supplemental results showing GLI1 as a relay connector between pSMAD2/3**

577   **and SNAIL1.** (A) Network of TGF-β activating SNAIL1 reconstructed with IPA. (B) Scatted

578   plot of measured nuclear GLI1 and SNAIL1 concentrations and the corresponding histogram

579   representation for [nuclear SNAIL1]. The same sets of data of Fig. 2C are used. (C) The model

580   of Fig. 2A with GLI1 reproduces the observed pSMAD2/3-SNAIL1 dynamics. To fit the

581   SNAIL1 dynamics the exact temporal profile of GLI1 is not important except the requirement of

582   its activation after 24 h. (D) Predicted outcome of adding GLI1 inhibitor at different time after

583   TGF-β1 treatment (blue lines). The red line is the predicted dynamics without the inhibitor. (E)

584   Fold change of *GLI1* mRNA levels measured with quantitative RT-PCR at different time points

585   after combined TGF-β1 treatment. (F) Fold change of *SNAIL1* mRNA levels measured with

586   quantitative RT-PCR after combined TGF-β1 and GLI1 inhibitor GANT61 treatment. For early

587   inhibition the inhibitor was added at the time of starting TGF-β1 treatment. For late inhibition

588   the inhibitor was added 48 h (for MCF7) and 24 h (for A549) after starting TGF-β1 treatment,

589   respectively.

590

591   **Figure S3 Supplemental results showing temporal switch between two phosphorylation**

592   **forms of GSK3.** (A) IF images showing the temporal switch between two phosphorylation forms

593   of GSK3. (B) Scattered plots showing correlation between nuclear and cytosol concentrations of

594   GSK3^D. (C) Immunoprecipitation studies showing two phosphorylation forms do not coexist.

595   Data of two replicas was shown. (D) Silver staining measurement of the relative amount of

27

596   different GSK3 forms. The right figure shows a representative of three independent replicates. M

597   refers to the marker indicating protein mass.

598

599   **Figure S4. Supplemental results of the full model.** (A) The model of Fig. 4A reproduces the

600   observed GLI1 as well as pSMAD2/3-SNAIL1 dynamics. (B) Examples of regulatory factors

601   having positive feedback loop and reservoir of molecules in inactive form that can be activated

602   by another stimulus. IDPs refer to intrinsically disordered proteins, and some of them are

603   transcription factors, which change into folded form and have higher DNA binding affinity upon

604   binding of cofactors or posttranslational modification. ID1 is a member of the family of

605   inhibitors of DNA binding proteins. (C) Bifurcation diagram showing that the initial

606   concentration boost is small compared to the concentration jump associated with external signal

607   induced switch of cell states. (D-E) Schematics of the early and full GSK3 inhibition

608   experiments.

609

610   **Figure S5** (A) Supplemental model results of pulsed TGF-β treatments with various mutations.

611   (B) Examples of other signaling transduction pathways that share similar motifs as TGF-β,

612   including IL-12, DNA double strand breaking, and LPS, in which extracellular signal is

613   transmitted through a canonical pathway with negative feedbacks and multiple non-canonical

614   pathways, and these pathways crosstalk at multiple points.

615

616   **Supplementary Movie S1: Subcellular localization of GSK3^{AA} (red).** Movies were composed

617   from z-stack imaging.

28

618   **Supplementary Movie S2: Subcellular localization of GSK3^{AA} (red) overlaid with ERC**

619   **(green) and DAPI (blue, nuclear area).** Movies were composed from z-stack imaging.
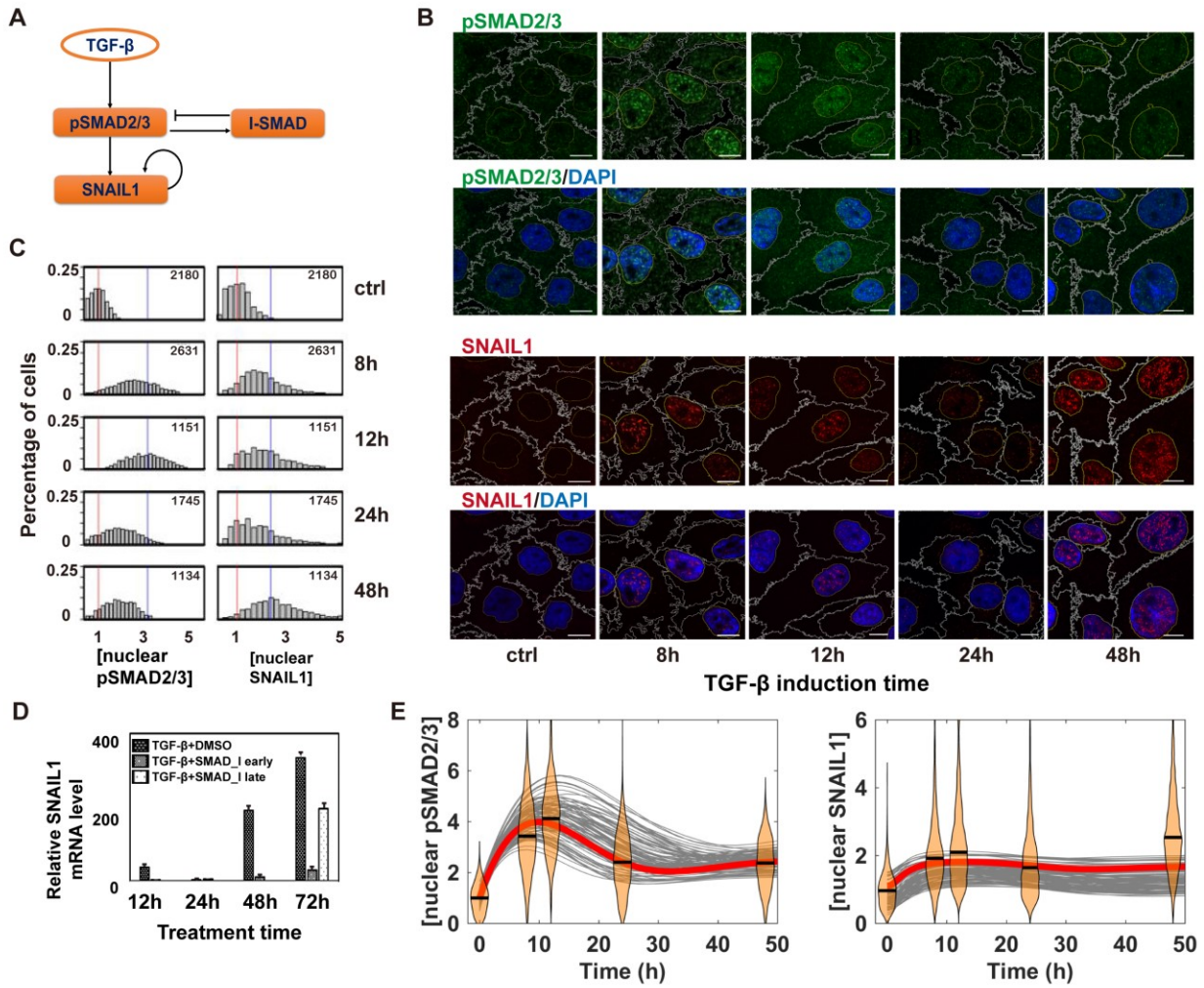
620

621

622   **Figure 1**

Figure 2

623
624

625

626

627

628   **Figure 3**

32

629

630   **Figure 4**

631

632   **Figure 5**

34

633

634   **Figure S1**

35

A

635

636   **Figure S2**

36

637   .
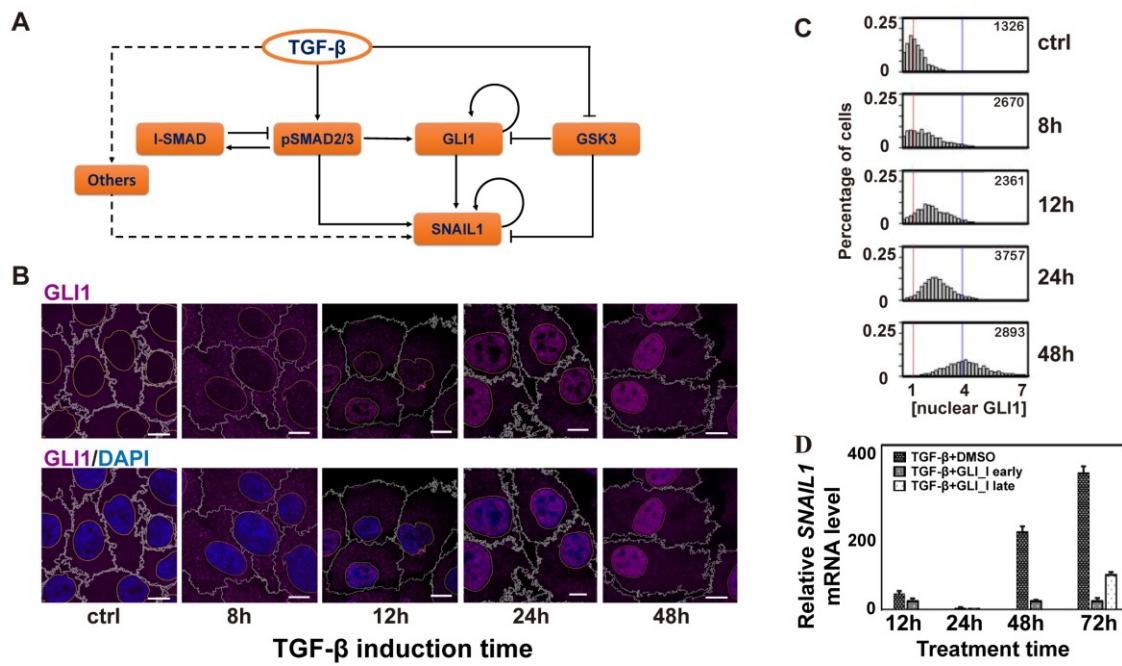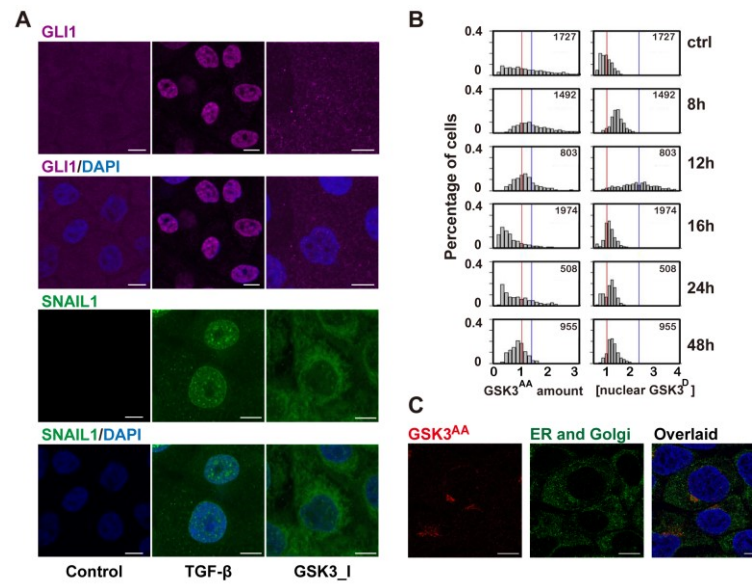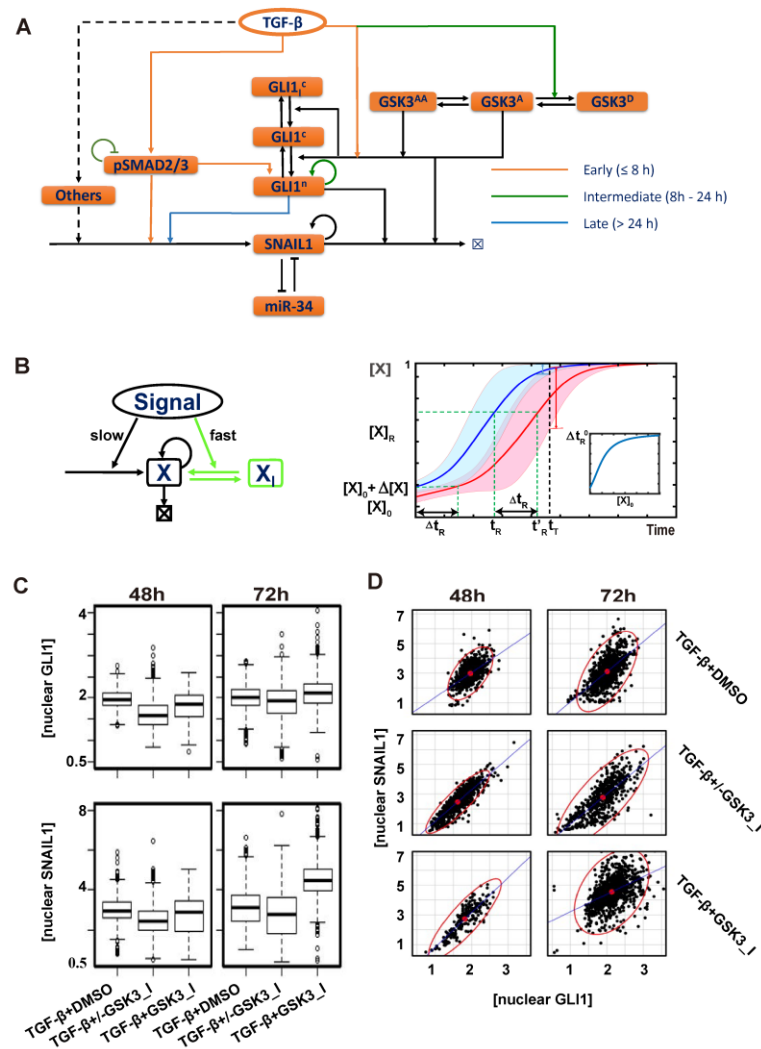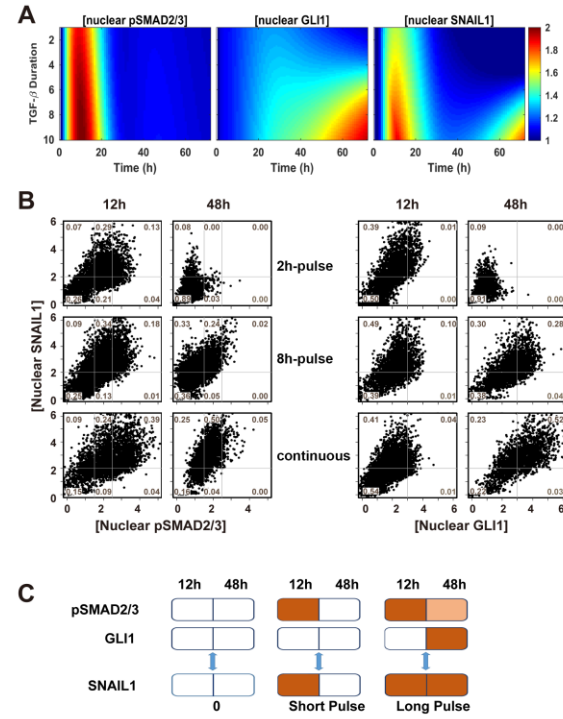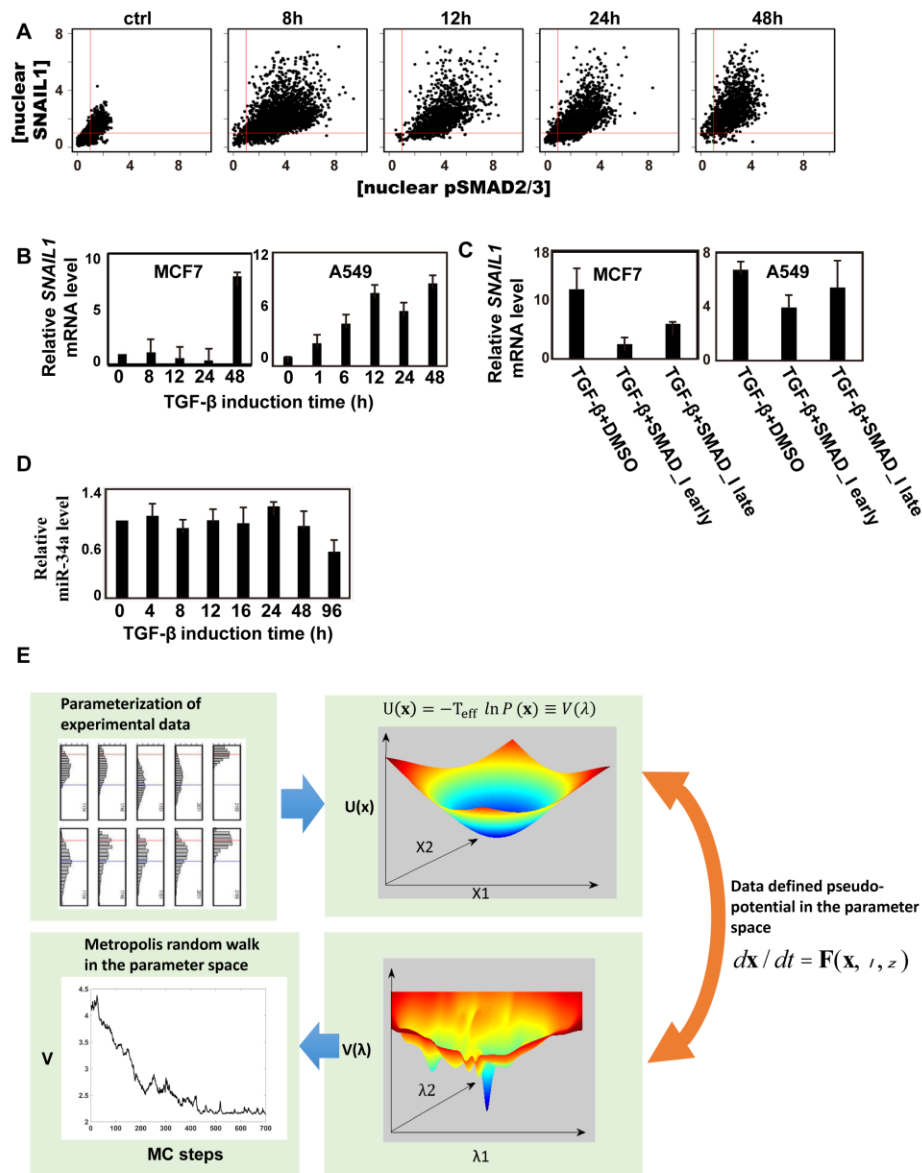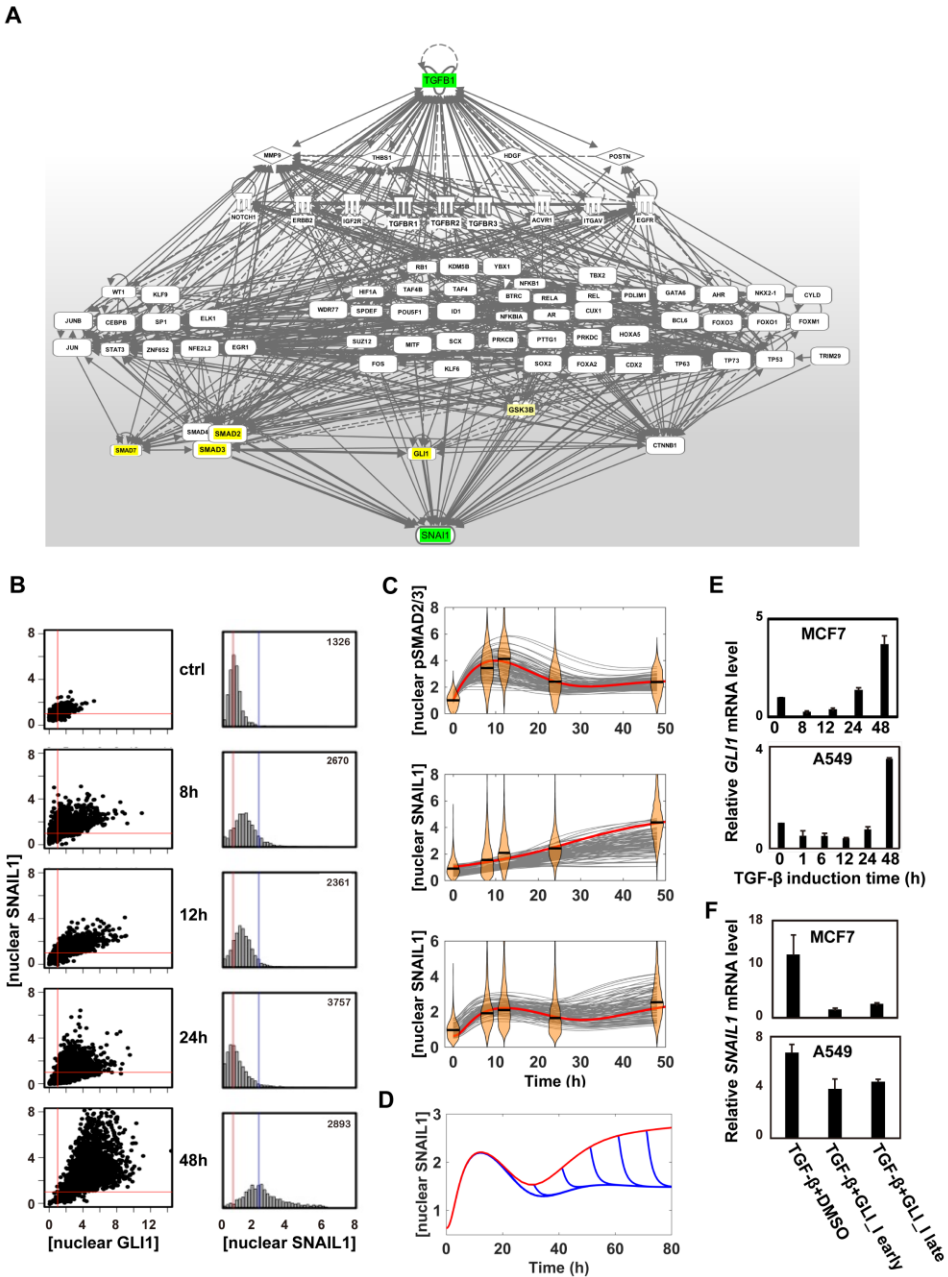
638   **Figure S3**

Figure S4

639

640

38

641

642   **Figure S5**

643

Supplementary Materials

Mathematical modeling

Canonical TGF-β/pSMAD2/3/SNAIL1 pathway (Fig. 1A)

647   We used this ordinary differential equation (ODE) model in Fig. 1 and Fig. S1.

TGF-β/SMAD2/3 module.

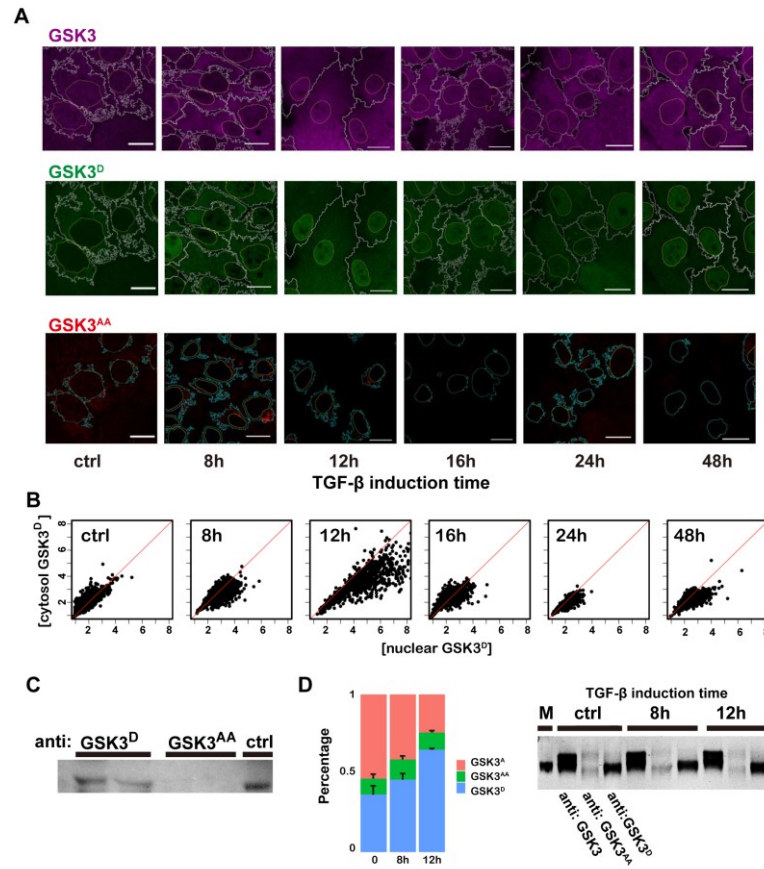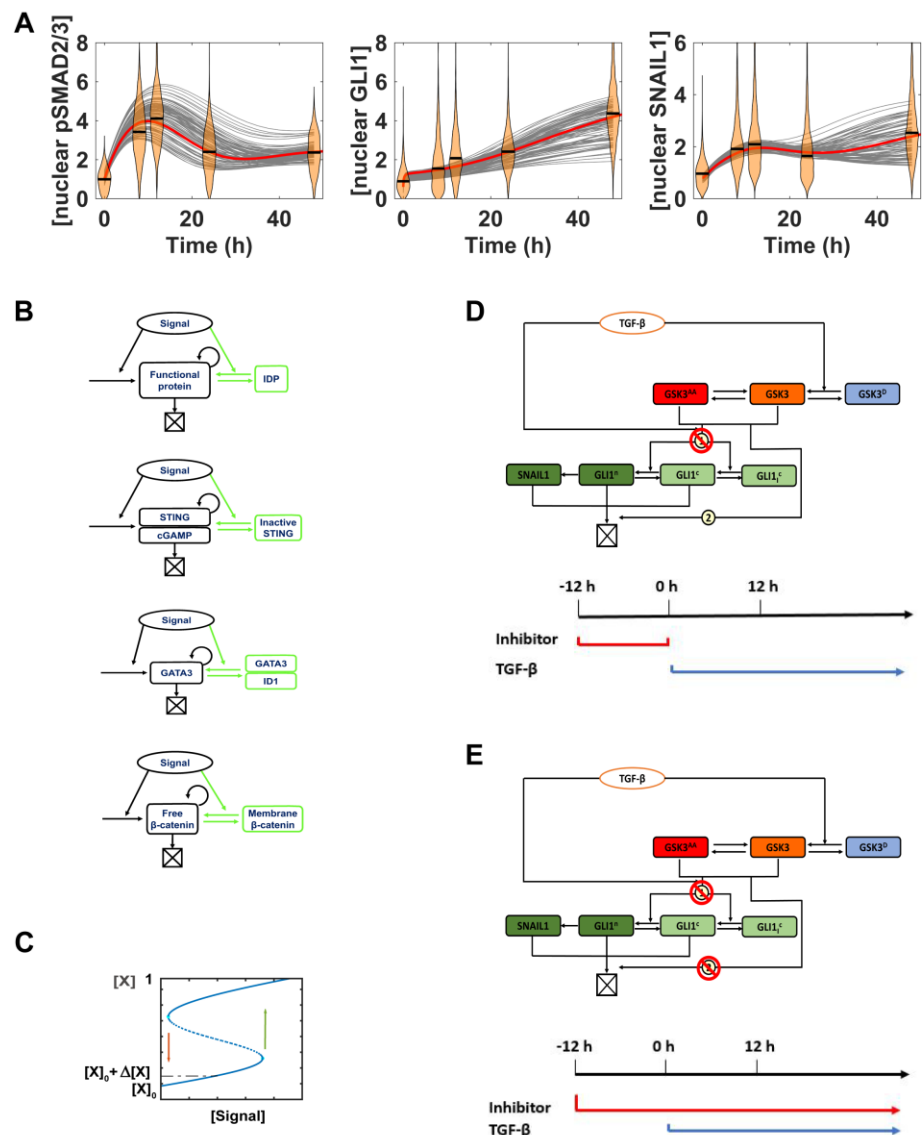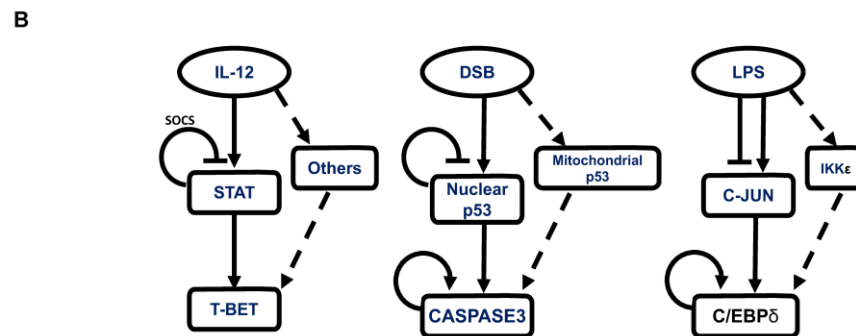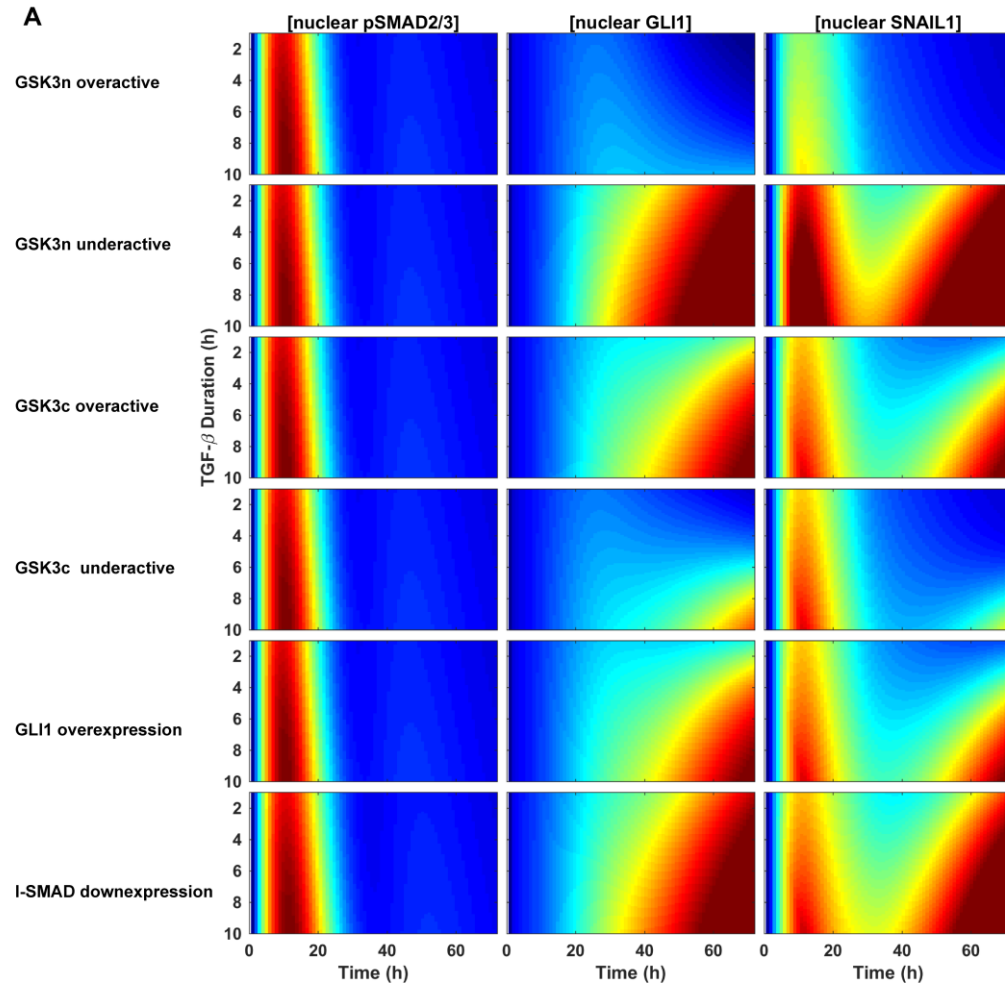649 $$[\text{Smad}]' = (\text{kp}_{smad0} + \text{kp}_{smad} * \text{TGF}) * \frac{\text{Smad}_{all} - [\text{Smad}]}{\text{Jp}_{smad0} + (\text{Smad}_{all} - [\text{Smad}])} \frac{1}{1 + \frac{\text{Smad}_I}{\text{Jdp}_{smad1}}} - \text{dp}_{smad}$$

650    $$* \frac{[\text{Smad}]}{\text{Jdp}_{smad} + [\text{Smad}]},$$

651    $$[\text{Smad}_I]' = \text{k}_{SmadI} * [\text{Smad}] - \text{kd}_{SmadI} * [\text{Smad}_I],$$

652   where [Smad] and $[\text{Smad}_I]$ are the concentrations of pSMAD2/3 and inhibitory SMAD, respectively.

653   **SNAIL-miR-34 module.** It is expanded from our previous model [20] by considering transcription
654   activation of SNAIL1 by pSMAD2/3 and TGF-β, and degradation of SNAIL1.

655    $$[\text{snail}]'_n = \text{k0}_{snail} + \text{k}_{snail0} * \frac{[\text{Smad}]^2}{\text{J}^2_{snail0} + [\text{Smad}]^2} \frac{1}{1 + \frac{[\text{SNAIL}]}{\text{J}_{snail2}}} - \text{kd}_{snail} * [\text{snail}] - \text{kd}_{SR1} * [\text{SR1}],$$

656    $$[\text{miR34}]'_n = \text{k0}_{34} + \frac{\text{k}_{34}}{1 + \left(\frac{\text{SNAIL}}{\text{J1}_{34}}\right)^2} - \text{kd}_{34} * [\text{miR34}] - (1 - \lambda_s) * \text{kd}_{SR1} * [\text{SR1}],$$

657    $$[\text{SNAIL}]' = \text{k}_{SNAIL} * [\text{snail}] - \text{kd}_{SNAIL} * [\text{SNAIL}],$$

658    $$[\text{miR34}] = [\text{miR34}]_t - [\text{SR1}],$$

659    $$[\text{snail}] = [\text{snail}]_t - [\text{SR1}],$$

660    $$[\text{SR1}] = \text{Ks} * [\text{snail}] * [\text{miR34}],$$

661 where [snail], [miR34], [SNAIL], [snail], [SR1] are the concentrations of total *SNAIL1* mRNA, miR-34,

662 SNAIL1 protein, free *SNAIL1* mRNA and miR-34-*SNAIL1* mRNA complex, respectively.

Canonical TGF-β/SMAD/SNAIL1 pathway with GLI1 (Fig. S2)

664 Taking into account the GLI1 self-activation and GLI1 mediated expression of *SNAIL1* mRNA, we added

665 another ODE for GLI1 and revised the ODE of *SNAIL1* mRNA.

666 $$[GLI]_n' = k_{gli0} + k_{gli1} * \frac{[Smad]^2}{J_{gli1}^2 + [Smad]^2} + k_{gli2} * \frac{[GLI]_n^2}{[GLI]n^2 + J_{gli2}^2} - d_{gli} * [GLI]_n,$$

667 $$[snail]_t' = k0_{snail} + \left(k_{snail0} * \frac{[Smad]^2}{J_{snail0}^2 + [Smad]^2} + k_{snail1} * \frac{[GLI]_n^m}{[GLI]_n^2 + J_{snail1}^m}\right) \frac{1}{1 + \frac{[SNAIL]}{J_{snail2}}} - kd_{snail} * [snail] -$$

668 $$kd_{SR1} * [SR1],$$

669 where $[GLI]_n$ is the concentration of nuclear GLI1. We used this ODE model to generate results in Fig.

670 S2.

Model for the GSK3/GLI module (Fig. 4A)

672 Since the process involves many steps and a detailed model would require many parameters to determine,

673 instead we used two phenomenological time-dependent functions to qualitatively mimic the dynamics of

674 the enzyme activities of cytosol GSK3 and nuclear GSK3 we experimentally measured,

675 $$[GSK]_c(t) = k_{GSKc} * TGF * \left(1 - \exp\left(-\frac{t}{a1}\right)\right) * \exp\left(-\frac{t - b1}{a1}\right),$$

676 $$[GSK]_n(t) = 1 - k_{GSKn} * TGF * \left(1 - \exp\left(-\frac{t}{a2}\right)\right) * \left(\exp\left(-\frac{t - b2}{a2}\right)\right).$$

677 Furthermore, the basal pool of cytosol GLI1 is considered, which is by sequestered in the cytosol by Sufu

678 but could translocate to the nuclear after Sufu is inactivated by the cytosol enzyme GSK3 activity. We

679 used a revised ODE of nuclear GLI1 concentration derived with the quasi-equilibrium approximation (see

680 below)

41

681     $[GLI]_t' \approx k_{gli0} + k_{gli1} * \dfrac{[Smad]^2}{J_{gli1}^2 + [Smad]^2} + k_{gli2} * \dfrac{[GLI]_n^{nm}}{[GLI]_n^m + J_{gli2}^m} - d_{gli} * [GLI]_n * [GSK]_n;$

682     $[GLI]_n = \dfrac{[GSK]_c + K1}{(K3+1)[GSK]_c + K1 + K4} [GLI]_t$

Derivation of GLI ODE,

684   We assumed the quasi-equilibrium approximation for the GLI nuclear and cytosol shuttling, the GSK3

685   regulated binding/unbinding between Sufu and GLI in the cytosol, and obtained the following equations,

686     $K2 * [GLI]_c * [Sufu] = (K1 + [GSK]_c) * [GLIsufu],$

687     $[GLIsufu] = Sufu_{max} - [Sufu]$

688   Thus we have

689     $[GLIsufu] = Sufu_{max} - (K1 + [GSK]_c) * \dfrac{[GLIsufu]}{K2 * [GLI]_c}$

690   That is,

691     $[GLIsufu] = \dfrac{1}{1 + \dfrac{(K1 + [GSK]_c)}{K2 * [GLI]_c}} Sufu_{max}$

692   Also we have $[GLI]_c = K3 * [GLI]_n$, thus

693     $[GLIsufu] = \dfrac{K3 * K2 * [GLI]_n}{K3 * K2 * [GLI]_n + (K1 + [GSK]_c)} Sufu_{max}$

694   The total level of GLI1 is the sum of the three forms, GLISufu, GLI_c and GLI_n,

695     $[GLI]_t = [GLI]_c + [GLI]_n + [GLIsufu] = \left(K3 * [GLI]_n + [GLI]_n + \dfrac{K2*K3*[GLI]_n}{K3*K2*[GLI]_n+(K1+[GSK]_c)} Sufu_{max} \right).$

696   Thus, we obtained the relation among $[GLI]_n$, $[GLI]_t$ and $[GSK]_c$

697     $[GLI]_n = f(GSK_c, [GLI]_t) ,$

42

698   The total concentration of GLI1 is given by,

699    $[\text{GLI}]_t{}' = k_{\text{gli0}} + k_{\text{gli1}} * \dfrac{[\text{Smad}]^2}{J_{\text{gli1}}^2 + [\text{Smad}]^2} + k_{\text{gli2}} * \dfrac{[\text{GLI}]_n{}^m}{[\text{GLI}]_n{}^m + J_{\text{gli2}}^m} - d_{\text{gli}} * [\text{GLI}]_c * [\text{GSK}]_c - d_{\text{gli}}$

700                    $* [\text{GLI}]_n * [\text{GSK}]_n.$

701   Given that our data shows that $[\text{GLI}]_c$ is low throughout the process, we neglected the degradation term of

702    $[\text{GLI}]_c$,

703    $[\text{GLI}]_t{}' \approx k_{\text{gli0}} + k_{\text{gli1}} * \dfrac{[\text{Smad}]^2}{J_{\text{gli1}}^2 + [\text{Smad}]^2} + k_{\text{gli2}} * \dfrac{[\text{GLI}]_n{}^m}{[\text{GLI}]_n{}^m + J_{\text{gli2}}^m} - d_{\text{gli}} * [\text{GLI}]_n * [\text{GSK}]_n$

704   **TGF-β pulse**

705   Since TGF-β1 can enter to cells through endocytosis, washing the extracellular TGF-β1 does not stop the

706   signaling immediately. Therefore, we modeled the effective TGF-β1 concentration by the following

707   equation,

708    $[\text{TGF}](t) = \text{TGF}_0 * \exp\big(-d_{\text{tgf}} * (t - \text{TGF}_{\text{Duration}}) * \text{Heaviside}(t - \text{TGF}_{\text{Duration}}) \big).$

709   **Full model**

710   By considering all the modules, the full model is as following,

711    $[\text{Smad}]' = (kp_{\text{smad0}} + kp_{\text{smad}} * [\text{TGF}]) * \dfrac{\text{Smad}_{\text{all}} - [\text{Smad}]}{Jp_{\text{smad0}} + (\text{Smad}_{\text{all}} - [\text{Smad}])} \dfrac{1}{1 + \dfrac{[\text{Smad}_I]}{Jdp_{\text{smad1}}}} - dp_{\text{smad}}$

712                    $* \dfrac{[\text{Smad}]}{Jdp_{\text{smad}} + [\text{Smad}]},$

713    $[\text{Smad}_I]' = k_{\text{SmadI}} * [\text{Smad}] - kd_{\text{SmadI}} * [\text{Smad}_I],$

714    $[\text{GLI}]_t{}' = k_{\text{gli0}} + k_{\text{gli1}} * \dfrac{\text{Smad23}^2}{J_{\text{gli1}}^2 + \text{Smad23}^2} + k_{\text{gli2}} * \dfrac{[\text{GLI}]_n{}^m}{[\text{GLI}]_n{}^m + J_{\text{gli2}}^m} - d_{\text{gli}} * [\text{GLI}]_c * [\text{GSK}]_c - d_{\text{gli}}$

715                    $* [\text{GLI}]_n * [\text{GSK}]_n,$

43

716 $\quad [\text{snail}]_t{}' = \text{k0}_{\text{snail}} + \left(k_{\text{snail0}} * \frac{[\text{Smad}]^2}{J^2_{\text{snail0}} + [\text{Smad}]^2} + k_{\text{snail1}} * \frac{[\text{GLI}]_n{}^m}{[\text{GLI}]_n{}^m + J^m_{\text{snail1}}} \right) \frac{1}{1 + \frac{[\text{SNAIL}]}{J_{\text{snail2}}}} - \text{kd}_{\text{snail}} * [\text{snail}] -$

717 $\quad \text{kd}_{\text{SR1}} * [\text{SR1}],$

718 $\quad [\text{miR34}]_n' = \text{k0}_{34} + \dfrac{k_{34}}{1 + \left(\frac{\text{SNAIL}}{J1_{34}}\right)^2} - \text{kd}_{34} * [\text{miR34}] - (1 - \lambda_s) * \text{kd}_{\text{SR1}} * [\text{SR1}],$

719 $\quad [\text{SNAIL}]' = \text{k}_{\text{SNAIL}} * [\text{snail}] - \text{kd}_{\text{SNAIL}} * [\text{SNAIL}] * [\text{GSK}]_n,$

720 $\quad [\text{GSK}]_c(t) = \text{k}_{\text{GSKc}} * [\text{TGF}] * \left(1 - \exp\left(-\dfrac{t}{a1}\right) \right) * \exp\left(-\dfrac{t - b1}{a1}\right),$

721 $\quad [\text{GSK}]_n(t) = 1 - \text{k}_{\text{GSKn}} * [\text{TGF}] * \left(1 - \exp\left(-\dfrac{t}{a2}\right) \right) * \left(\exp\left(-\dfrac{t - b2}{a2}\right) \right),$

722 $\quad [\text{GLI}]_n = f([\text{GSK}]_c, [\text{GLI}]_t)$

723 $\quad [\text{miR34}] = [\text{miR34}]_t - [\text{SR1}],$

724 $\quad [\text{snail}] = [\text{snail}]_t - [\text{SR1}],$

725 $\quad [\text{SR1}] = \text{Ks} * [\text{snail}] * [\text{miR34}].$

726 $\quad$ We used this ODE model to generate results in Fig. 5 and Fig. S5A.

727 $\quad$ **Parameter space searching**

728 $\quad$ Step 1: Calculate single cell distributions of experimental observables. We calculated histograms of the

729 $\quad$ distributions from the single cell experimental data. Suppose that we have N observables measured in M

730 $\quad$ time points, we have an $N \times M$ dimensional distribution of the data. Since we used fixed cells and we had

731 $\quad$ no information on the temporal correlation, we treated the distributions from different time points as

732 $\quad$ independent, *i.e.*, $P = \prod_{i=1}^{M} P_i.$

733 $\quad$ Step 2: Define pseudo-potentials from the parameterized distribution. We defined a pseudo-scalar-

734 $\quad$ potential function $U(\mathbf{x}_1, \mathbf{x}_2, .., \mathbf{x}_M) = -T_{eff}(lnP - lnP_{max})$. The constant T_{eff} is an effective

735   temperature, which we chose $T_{eff} = 1$. The constant term $lnPmax$ sets the potential to be zero at the

736   peak position of the distribution, and does not affect the parameter space search results. This pseudo-

737   potential is just an auxiliary scalar function for the following application of the Metropolis algorithm. If a

738   mathematical model can faithfully describe the system dynamics, with given initial conditionals and non-

739   adjustable parameter set of ζ, we should be able to find distributions of the parameter set λ (to take into

740   account cell-to-cell heterogeneity), and generate the corresponding distributions of $(\mathbf{x}_1, \mathbf{x}_2, .., \mathbf{x}_M)$ to

741   reproduce U. That is, for a specific set of λ, $\mathbf{x}_i = \mathbf{x}_i (\mathbf{x}_0; \lambda, \zeta), i = 1, ... M$, and $U(\mathbf{x}_1, \mathbf{x}_2, .., \mathbf{x}_M) \equiv$

742   $V(\lambda)$. Unlike U, the function form of V can be very complex, but fortunately we do not need to know its

743   explicit function form to perform the following Metropolis sampling.

744   Step 3: Obtain model parameter distributions that reproduce the distributions of experimental observables.

745   Now it is clear why we define the pseudo-potential. We performed Monte Carlo random walks along the

746   pseudo-potential V in the λ space using the Metropolis algorithm, just as how the algorithm is typically

747   applied along real physical potentials. At each step with a set of λ, we generated a trial move $\lambda' = \lambda + \delta\lambda$.

748   We propagated the ODEs to obtain $V(\lambda)$ and $V(\lambda')$, then use the Metropolis criteria to decide whether to

749   accept the new move. If $V(\lambda') \leq V(\lambda)$ accept this step and update the parameter set $\lambda = \lambda'$. If $V(\lambda') >$

750   $V(\lambda)$, accept this step with a probability $\exp(-(V(\lambda') - V(\lambda))/T)$, with $T = 1$.

751   In our model, there is no feedback between the SMAD2/3 module and the SNAIL1/miR-34 module, thus

752   we used a two-step to searching the parameter space for the TGF-β/SMAD2/3 module,

753   1.   Search the parameter space (nine parameters) in the SMAD2/3 module;

754   2.   Search the parameter space (six parameters) for the SNAIL1/miR-34 module based on the 50 samples

755   of good-fit parameter set of the SMAD2/3 module from step 1.

756   In step 2 some of the parameters in the SNAIL1/miR-34 module were fixed and used as a well-trained

757   parameter set from our previous work [20]. Instead only six new parameters that connect the module

758   SMAD2/3 and module SNAIL1/miR-34 were considered in the parameter space searching.

759   When the GLI1 module was included, we again used the fact that there is no feedback between the

760   SMAD2/3 module and the GLI1 module, and used a three-step searching procedure to reduce the

761   computational efforts,

762   1. Search the parameter space (nine parameters) for the SMAD2/3 module;

763   2. Search the parameter space (seven parameters) for the GLI1 module;

764   3. Search the parameter space (six parameters) for the SNAIL1/miR-34 module based on the 50 samples

765   of good-fit parameter set of the SMAD2/3 module the GLI1 module from step 1-2.

766   **Parameter change in various over-expression/down-expression or over-active/down-active**

767   **conditions (Fig. S5)**

768   To produce the results in Fig. S5A, a 1.2-fold change of k_{gli0} is used in the case of GLI1 over-expression,

769   a 0.8-fold change of k_{smadi} in the case of I-SMAD down-regulation. There is 0.8-fold change of k_{gskn} in

770   the case of over-active cytosol GSK3, 1.2-fold change of k_{gskn} in the case of under-active cytosol GSK3.

771   Similarly, there is 1.2-fold change of k_{gskc} in the case of over-active nuclear GSK3, and 0.5-fold change

772   of k_{gskc} in the case of under-active nuclear GSK3.

773

774   **Supplementary Table 1. Primer list**

Primers	Sequence	References
SNAIL1_QRT_F	ATCGGAAGCCTAACTACAGCGA	41
SNAIL1_QRT_R	CACGCCTGGCACTGGTACTTCT	
GLI1_QRT_F	CTCCCTCGTAGCTTTCATCAAC	
GLI1_QRT_F	GTGCTCGCTGTTGATGTGGTG	
GAPDH_QRT_F	ACCACAGTCCATGCCATCAC	41
GAPDH_QRT_F	TCCACCACCCTGTTGCTGTA	
Stem_loop_Uni	GTCGTATCCAGTGCAGGGTCCGAGGTATTCGCACTGGATACGAC	42
miR-34a-5p_SL	GTCGTATCCAGTGCAGGGTCCGAGGTATTCGCACTGGATACGACACAACC	
Universal_primer	CCAGTGCAGGGTCCGAGGTA	
miR-34a-5p_RT	CACGCATGGCAGTGTCTTAGC	

775

776

47

777 **Supplementary Table 2. The Parameters values of the best fit of the full model.**

Parameter	Description	Value
TGF-β/SMAD2/3 module		
kp_smad0	Basal activation rate of SMAD2/3	1.5778 µM/hr
kp_smad	TGF-β dependent activation rate of SMAD2/3	0.2675 µM/hr
$Smad_{all}$	The total level of SMAD2/3	27.5377 µM
dp_smad	Deactivation rate of SMAD2/3	1.4833 µM/hr
Jp_smad0	Michaelis constant of SMAD2/3 activation	0.4198 µM
Jdp_smad	Michaelis constant of SMAD2/3 deactivation	0.3639 µM
Jp_smad1	Michaelis constant of SMAD-I mediated inhibition of SMAD2/3 activation	0.8326 µM
k_smadi	Expression rate of inhibitory SMAD	0.0254 µM/hr
kd_smadi	Degradation rate of inhibitory SMAD	0.0710 µM/hr
GSK3 /GLI1 module		
k_GSKc	The activation rate of cytosol GSK3[AA] enzyme activity	1/hr
k_GSKn	The deactivation rate of nuclear GSK3 enzyme activity	0.25/hr
a1	Constant a of cytosol GSK3 enzyme activity	10
b1	Constant b of cytosol GSK3 enzyme activity	10
a2	Constant a of nuclear GSK3 enzyme activity	20
b2	Constant b of nuclear GSK3 enzyme activity	20
k_gli0	Basal transcription rate of *gli1*	0.0003 µM/hr
k_gli1	SMAD2/3-dependent transcription rate of *gli1*	0.0453 µM/hr
k_gli2	GLI1-dependent transcription rate of *gli1*	0.2288 µM/hr

48

d_gli	Degradation rate of GLI1	0.0166 /hr
J_gli1	Michaelis constant of SMAD2/3 -dependent transcription of *gli1*	0.7563 μM
J_gli2	Michaelis constant of GLI1-dependent transcription of *gli1*	2.4192 μM
SNAIL1/miR-34 module		
$k0_{snail}$	Basal transcription rate of *snail1*	0.0034 μM/hr
k_{snail0}	SMAD2/3-dependent transcription rate of *snail1*	1.3942 μM/hr
k_{snail1}	GLI1-dependent transcription rate of *snail1*	43.5453 μM/hr
J_{snail0}	Michaelis constant of SMAD2/3-dependent *snail1* transcription	0.7522 μM
J_{snail1}	Michaelis constant of GLI1-dependent *snail1* transcription	7.2215 μM
J_{snail1}	Michaelis constant of SNAIL1-dependent *snail1* transcription inhibition	0.2012 μM
kd_{snail}	Degradation rate of *SNAIL1* mRNA	0.09 /hr
kd_{SR}	Degradation rate of miR34-*SNAIL1* complex	0.9 /hr
k_{SNAIL}	Translation rate of *SNAIL1* mRNA	17 μM/hr
kd_{SNAIL}	Degradation rate of SNAIL1	1.66 /hr
$k0_{34}$	Basal production rate of miR-34	0.0012 μM/hr
k_{34}	Production rate of miR-34	0.012 μM/hr
$J1_{34}$	Michaelis constant of SNAIL1-dependent inhibition of miR-34 production	0.15 μM
kd_{34}	Degradation rate of miR-34	0.035 /hr
K_s	Affinity constant of miR-34 and *SNAIL1* mRNA	100 /μM
λs	Recycle ratio of miR-34	0.5

778   **The parameters shaded are searched with our algorithm.**

49

Reference

1.   Albeck, J.G., Mills, G.B. & Brugge, J.S. Frequency-modulated pulses of ERK activity transmit quantitative proliferation signals. *Mol Cell* **49**, 249-261 (2013).

2.   English, J.G. *et al.* MAPK feedback encodes a switch and timer for tunable stress adaptation in yeast. *Sci Signal* **8**, ra5 (2015).

3.   Fu, Y. *et al.* Reciprocal encoding of signal intensity and duration in a glucose-sensing circuit. *Cell* **156**, 1084-1095 (2014).

4.   Kholodenko, B.N. Cell-signalling dynamics in time and space. *Nat Rev Mol Cell Biol* **7**, 165-176 (2006).

5.   Nathan, C. Points of control in inflammation. *Nature* **420**, 846-852 (2002).

6.   Massagué, J. TGFβ signalling in context. *Nat Rev Mol Cell Biol* **13**, 616-630 (2012).

7.   Massagué, J. How cells read TGF-β signals. *Nat Rev Mol Cell Biol* **1**, 169-178 (2000).

8.   Borthwick, L.A. & Wynn, T.A. IL-13 and TGF-β1: core mediators of fibrosis. *Curr Pathobiol Rep* **3**, 273-282 (2015).

9.   Lamouille, S., Xu, J. & Derynck, R. Molecular mechanisms of epithelial-mesenchymal transition. *Nat Rev Mol Cell Biol* **15**, 178-196 (2014).

10.   Wu, M.Y. & Hill, C.S. Tgf-β superfamily signaling in embryonic development and homeostasis. *Dev Cell* **16**, 329-343 (2009).

11.   Moses, H.L., Roberts, A.B. & Derynck, R. The discovery and early days of TGF-β: A historical perspective. *Cold Spring Harb Perspect Biol* **8**, a021865 (2016).

12.   Fabregat, I., Fernando, J., Mainez, J. & Sancho, P. TGF-β signaling in cancer treatment. *Curr Pharm Des* **20**, 2934-2947 (2014).

13.   Colak, S. & ten Dijke, P. Targeting TGF-β signaling in cancer. *Trends in Cancer* **3**, 56-71 (2017).

14.   Vizán, P. *et al.* Controlling long-term signaling: receptor dynamics determine attenuation and refractory behavior of the TGF-β pathway. *Sci Signal* **6**, ra106 (2013).

15.   Warmflash, A. *et al.* Dynamics of TGF-β signaling reveal adaptive and pulsatile behaviors reflected in the nuclear localization of transcription factor Smad4. *Proc Natl Acad Sci USA* **109**, E1947-1956 (2012).

16.   Zi, Z. *et al.* Quantitative analysis of transient and sustained transforming growth factor-β signaling dynamics. *Mol Syst Biol* **7**, 492 (2011).

17.   Xu, J., Lamouille, S. & Derynck, R. TGF-β-induced epithelial to mesenchymal transition. *Cell Res* **19**, 156-172 (2009).

18.   Thuault, S. *et al.* HMGA2 and Smads co-regulate SNAIL1 expression during induction of epithelial-to-mesenchymal transition. *J Biol Chem* **283**, 33437-33446 (2008).

19.   Schmierer, B., Tournier, A., Bates, P. & Hill, S. Mathematical modeling identifies Smad nucleocytoplasmic shuttling as a dynamic signal-interpreting system. *Proc Natl Acad Sci USA* **105**, 6608-6613 (2008).

20.   Zhang, J. *et al.* TGF-β-induced epithelial-to-mesenchymal transition proceeds through stepwise activation of multiple feedback loops. *Sci Signal* **7**, ra91-ra91 (2014).

21.   Aomatsu, K. *et al.* TGF-β induces sustained upregulation of SNAI1 and SNAI2 through Smad and non-Smad pathways in a human corneal epithelial cell line. *Invest Ophthalmol Vis Sci* **52**, 2437-2443 (2011).

22.   Dennler, S. *et al.* Induction of sonic hedgehog mediators by transforming growth factor-β: Smad3-dependent activation of Gli2 and Gli1 expression in vitro and in vivo. *Cancer Res* **67**, 6981-6986 (2007).

824   23.   Javelaud, D. *et al.* TGF-β/SMAD/GLI2 signaling axis in cancer progression and metastasis. *Cancer*
825   *Res* **71**, 5606-5610 (2011).
826   24.   Steinway, S.N. *et al.* Network modeling of TGFβ signaling in hepatocellular carcinoma epithelial-
827   to-mesenchymal transition reveals joint sonic hedgehog and Wnt pathway activation. *Cancer*
828   *Res* **74**, 5963-5977 (2014).
829   25.   Schlessinger, K. & Hall, A. GSK-3β sets Snail's pace. *Nat Cell Biol* **6**, 913-915 (2004).
830   26.   Mizuarai, S., Kawagishi, A. & Kotani, H. Inhibition of p70S6K2 down-regulates Hedgehog/GLI
831   pathway in non-small cell lung cancer cell lines. *Mol Cancer* **8**, 44 (2009).
832   27.   Hughes, K., Nikolakaki, E., Plyte, S.E., Totty, N.F. & Woodgett, J.R. Modulation of the glycogen
833   synthase kinase-3 family by tyrosine phosphorylation. *EMBO J.* **12**, 803-808 (1993).
834   28.   Meares, G.P. & Jope, R.S. Resolution of the nuclear localization mechanism of glycogen synthase
835   kinase-3: functional effects in apoptosis. *J Biol Chem* **282**, 16989-17001 (2007).
836   29.   Takenaka, K., Kise, Y. & Miki, H. GSK3β positively regulates Hedgehog signaling through Sufu in
837   mammalian cells. *Biochem Bioph Res Co* **353**, 501-508 (2007).
838   30.   Cole, A., Frame, S. & Cohen, P. Further evidence that the tyrosine phosphorylation of glycogen
839   synthase kinase-3 (GSK3) in mammalian cells is an autophosphorylation event. *Biochem J* **377**,
840   249 (2004).
841   31.   Selimkhanov, J. *et al.* Accurate information transmission through dynamic biochemical signaling
842   networks. *Science* **346**, 1370-1373 (2014).
843   32.   Cheong, R., Rhee, A., Wang, C.J., Nemenman, I. & Levchenko, A. Information Transduction
844   Capacity of Noisy Biochemical Signaling Networks. *Science* **334**, 354-358 (2011).
845   33.   Shirakihara, T., Saitoh, M. & Miyazono, K. Differential regulation of epithelial and mesenchymal
846   markers by δEF1 proteins in epithelial mesenchymal transition induced by TGF-β. *Mol Biol Cell*
847   **18**, 3533-3544 (2007).
848   34.   Fuxe, J., Vincent, T. & Garcia de Herreros, A. Transcriptional crosstalk between TGFβ and stem
849   cell pathways in tumor cell invasion: role of EMT promoting Smad complexes. *Cell Cycle* **9**, 2363-
850   2374 (2010).
851   35.   Aberger, F. & Ruiz, I.A.A. Context-dependent signal integration by the GLI code: the oncogenic
852   load, pathways, modifiers and implications for cancer therapy. *Semin Cell Dev Biol* **33**, 93-104
853   (2014).
854   36.   Doble, B.W. & Woodgett, J.R. GSK-3: tricks of the trade for a multi-tasking kinase. *J Cell Sci* **116**,
855   1175-1186 (2003).
856   37.   Kretschmer, A. *et al.* Differential regulation of TGF-β signaling through Smad2, Smad3 and
857   Smad4. *Oncogene* **22**, 6748-6763 (2003).
858   38.   Franco, D.L. *et al.* Snail1 suppresses TGF-β-induced apoptosis and is sufficient to trigger EMT in
859   hepatocytes. *J. Cell. Sci.* **123**, 3467-3477 (2010).
860   39.   Fabian, S.L. *et al.* Hedgehog-Gli pathway activation during kidney fibrosis. *Am J Pathol* **180**,
861   1441-1453 (2012).
862   40.   Carpenter, A.E. *et al.* CellProfiler: image analysis software for identifying and quantifying cell
863   phenotypes. *Genome Biol* **7**, R100 (2006).
864   41.   Zheng, X. *et al.* The transcription factor GLI1 mediates TGFβ1 driven EMT in hepatocellular
865   carcinoma via a SNAI1-dependent mechanism. *PloS One* **7**, e49581 (2012).
866   42.   Kramer, M.F. Stem-Loop RT-qPCR for miRNAs. *Curr Protoc Mol Biol*, 15.10. 11-15.10. 15 (2011).

867